Inorganic Chemistry
Cite This: Inorg. Chem. 2020, 59, 648−660
Article
pubs.acs.org/IC

Double-Oxalate-Bridging Tetralanthanide Containing Divacant Lindqvist Isopolytungstates with an Energy Transfer Mechanism and Luminous Color Adjustablility Through Eu^{3+}/Tb^{3+} Codoping

Xin Xu, Hailou Li, Saisai Xie, Ling Mei, Ruru Meng, Lijuan Chen,* and Junwei Zhao*

Henan Key Laboratory of Polyoxometalate Chemistry, College of Chemistry and Chemical Engineering, Henan University, Kaifeng, Henan 475004, China

Supporting Information

ABSTRACT: A double-oxalate-bridging tetra-Gd^{3+} containing divacant Lindqvist dimeric isopolytungtate $Na_{10}[Gd_2(C_2O_4)(H_2O)_4(OH)W_4O_{16}]_2{\cdot}30H_2O$ ($\mathbf{Gd_4W_8}$) was obtained based on the reaction of $Na_2WO_4{\cdot}2H_2O$, $H_2C_2O_4$, and $GdCl_3$ in aqueous solution. Its dimeric polyoxoanion is established by two divacant Lindqvist $[W_4O_{16}]^{8-}$ segments connected by a rectangular tetra-nuclearity $[Gd_4(C_2O_4)_2(H_2O)_8(OH)_2]^{6+}$ cluster. Notably, neighboring trinuclear $[Na_3O_4(H_2O)_{11}]^{5-}$ clusters are interconnected to construct a picturesque 1-D sinusoidal Na−O cluster chain. The most outstanding characteristic is that 1-D sinusoidal Na−O cluster chains combine $[Gd_2(C_2O_4)(H_2O)_4(OH)\text{-}W_4O_{16}]_2^{10-}$ polyoxoanions together, giving rise to an intriguing 3-D extended porous framework. The red emitter Eu^{3+} ions and green emitter Tb^{3+} ions are first codoped into $\mathbf{Gd_4W_8}$ to substitute Gd^{3+} ions for the exploration of the energy transfer (ET) mechanism between Eu^{3+} and Tb^{3+} ions and the color-tunable PL property in the isopolytungtate system. The PL emission spectra and decay lifetime measurements of the Eu^{3+}/Tb^{3+} codoped $\mathbf{Gd_4W_8}$ system illustrate that under excitation at 370 nm, Tb^{3+} ions can transfer energy to Eu^{3+} ions. When the molar concentration of Tb^{3+} ions is fixed at 0.9 and that of the Eu^{3+} ions gradually increases from 0.01 to 0.08, the calculated ET efficiency (η_{ET}) from Tb^{3+} to Eu^{3+} ions increases from 7.9% for $\mathbf{Gd_{0.36}Tb_{3.6}Eu_{0.04}W_8}$ to 67.3% for $\mathbf{Gd_{0.08}Tb_{3.6}Eu_{0.32}W_8}$. The energy transfer mechanism ($Tb^{3+} \rightarrow Eu^{3+}$) is a nonradiative dipole−dipole interaction. Furthermore, upon excitation at 370 nm, $\mathbf{Eu_4W_8}$ and $\mathbf{Tb_4W_8}$ show visible red- and green-emitting lights, respectively. When codoping trace amounts of Eu^{3+} ions in $\mathbf{Tb_4W_8}$, under excitation at 370 nm, $\mathbf{Tb_{3.92}Eu_{0.08}W_8}$ displays near white-light emission.

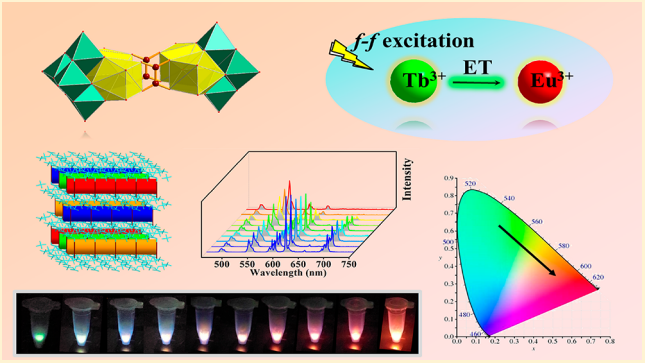

INTRODUCTION

Over the past few years, polyoxometalate-based inorganic−organic hybrid materials (POMIOHMs) have extensively caught the increasing attention of researchers owing to their complicated ingredients, peculiar bonding modes, and interesting frameworks relying on synergetic effects between inorganic and organic components.[1−7] Therein, polyoxometalates (POMs) exhibit superb nucleophilicity toward transition-metal (TM) and lanthanide (Ln) ions at specific sites and can function as the remarkable building blocks to construct unprecedented hybrid molecular materials.[8−12] Simultaneously, organic ligands also play a crucial role in constructing intriguing architectures and topologies of POMIOHMs. For instance, they have been used to overcome competitive reactions and induce aggregation of various TM or Ln centers.[13] Their abilities to link multivacant POM building blocks have also been reported.[14,15] Very recently, organic ligands have been employed as structure-directing agents and structural stabilizers.[16] Therefore, complicated components and unique structures of POMIOHMs usually determine their multidisciplinary applications in adsorption,[17] magnetism,[18] optics,[19] catalysis,[20] bioactivity,[21] and so forth.

Ln-based heteropolyoxotungstate inorganic−organic hybrid materials (Ln-HPOTIOHMs) have been an active research area in the past decade.[22] A large amount of work has been predominantly concentrated on di-, tri- and tetra-nuclear Ln-HPOTIOHMs with abundant structures and related properties.[19,23−33] However, very rare Ln-based isopolyoxotungstate inorganic−organic hybrid materials (Ln-IPOTIOHMs) have been reported (Figure S1).[34] It is also worthy of considering that the construction of Ln-HPOTIOHMs often relies on mono-, di-, and trivacant Keggin-type heteropolyoxotungstate segments; similarly, it is worth considering whether multivacant isopolyoxotungstate units with more nucleophilic oxygen atoms at vacant sites exist? It will be a challenge for the future evolutionary direction of Ln-IPOTIOHMs.

The suitable incorporation of Ln ions to POMs will give birth to novel optic properties such as electroluminescent

Received: September 29, 2019
Published: December 19, 2019

DOI: 10.1021/acs.inorgchem.9b02903
Inorg. Chem. 2020, 59, 648−660

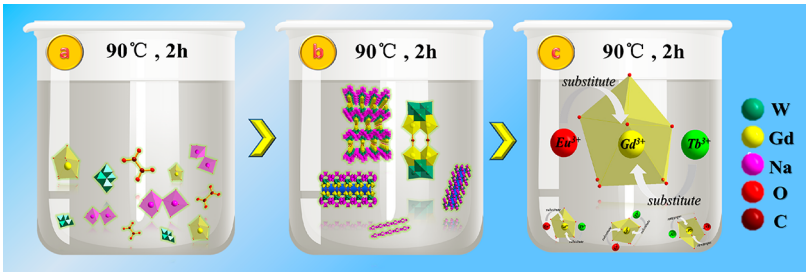

Figure 1. (a, b) Schematic synthetic procedure of $\mathbf{Gd_4W_8}$. (c) The process of Eu^{3+} and Tb^{3+} substituting Gd^{3+} ions in $\mathbf{Gd_4W_8}$.

materials, white-light-emitting diodes (W-LEDs), optical waveguide amplifiers, biosensing technologies, and imaging techniques,[35,36] which can be ascribed to high luminescence performances of Ln ions in POM system. (a) Ln ions can emit various sharp color emissions through *f*−*f* electron transitions;[37] (b) the luminescence emission of Ln ions can be sensitized by POM segments upon the O → W ligand-to-metal charge-transfer (LMCT) photoexcitation.[38] (c) Ln ions can be treated as an emitting sensitizer or antenna to transfer energy to the acceptor.[39,40] For example, in 2011, Boskovic's group researched the luminescence sensitization of inorganic POM and organic ligands to Tb^{3+} and Eu^{3+} ions.[28] In 2017, our group systematically explored luminescence behaviors of a series of serine-decorated Ln-substituted POMIOHMs.[13] However, these research reports mostly concentrate on homo-Ln incorporated POM materials, and numerous findings expound that homo-Ln incorporated POM materials already cannot satisfy with the needs of light-emitting materials due to some of their limitations such as high color drift, low luminescence intensity, and low photostability.[41,42] It has been certified that hetero-Ln codoped POM materials may resolve these problems, and few examples have been reported. For example, in 2018, Niu and co-workers reported Dy^{3+}/Er^{3+}-doped POM derivatives with near white-light-emitting behavior and high luminescence stability.[43] Our group prepared a series of Er^{3+}/Yb^{3+}-doped tellurotungstates to enhance the luminescence intensity of Er^{3+} ions through up-conversion luminescence regulation.[44] However, the approaches to figure out the ET between Ln ions and to obtain the near white-light-emitting POM materials are still immature.

The technology to obtain white-light emission has two methods. One is codoping blue-emitting Tm^{3+} and yellow-emitting Dy^{3+} into Ln-POMs with an appropriate ratio.[45] The other is dynamically tuning the emission ratio of red, green, and blue.[46] As we know, trivalent Eu^{3+} ions can perform as a great red emitter due to their sharp line emission ascribed to the $^5D_0 \rightarrow {}^7F_J$ transition. The Eu^{3+} ion occupies the asymmetric site, which not only emits yellow light at 595 nm ($^5D_0 \rightarrow {}^7F_1$) and orange light at 614 nm ($^5D_0 \rightarrow {}^7F_2$) but also reveals a good color rendering index.[47,48] Moreover, the Tb^{3+} ion can not only emit sharp green emission at 493 and 545 nm corresponding to the $^5D_4 \rightarrow {}^7F_6$ and $^5D_4 \rightarrow {}^7F_5$ transitions, respectively, but also function as an effective sensitizer for the Eu^{3+} emission.[49−52] What's more, energy transfer efficiency (η_{ET}) and multipolar interactions can be used to systematically unlock the ET mechanism between different Ln ions in a hetero-Ln-POM system,[53,54] which provide powerful support for exploring the ET mechanism and luminescence performances through codoping multiple Ln ions to Ln-POMs.

Herein, we synthesized a double-oxalate-bridging tetra-Gd-substituted isopolyoxotungstate-based inorganic−organic hybrid material (IPOTIOHM) $Na_{10}[Gd_2(C_2O_4)(H_2O)_4(OH)W_4O_{16}]_2{\cdot}30\,H_2O$ ($\mathbf{Gd_4W_8}$), which represents a rare example of Ln-IPOTIOHMs. The supramolecular stacking of $\mathbf{Gd_4W_8}$ reveals a 3-D multichannel framework when Na^+ cations perform as metal linkers, and the radii of each hole is about 4.40 Å. We first introduced various molar ratios of Eu^{3+} and Tb^{3+} ions to substitute Gd^{3+} ions in $\mathbf{Gd_4W_8}$ to prepare a series of derivatives $\mathbf{Gd_{4-4a}Eu_{4a}W_8}$ (a = 0.01, 0.02, 0.03, 0.04, 0.07, 0.10, 0.40, 0.70, 1.00), $\mathbf{Gd_{4-4b}Tb_{4b}W_8}$ (b = 0.01, 0.02, 0.03, 0.04, 0.07, 0.10, 0.40, 0.70, 1.00), $\mathbf{Gd_{0.4-4x}Eu_{4x}Tb_{3.6}W_8}$ (x = 0.00, 0.01, 0.02, 0.03, 0.04, 0.05, 0.06, 0.07, 0.08), and $\mathbf{Gd_{3.6-4y}Tb_{4y}Eu_{0.4}W_8}$ (y = 0.00, 0.10, 0.20, 0.30, 0.40, 0.50, 0.60, 0.70, 0.80) (Tables S1a−S1d). We also doped various amounts of Eu^{3+} ions into $Na_{10}[Tb_2(C_2O_4)(H_2O)_4(OH)W_4O_{16}]_2{\cdot}30H_2O$ ($\mathbf{Tb_4W_8}$) to obtain $\mathbf{Tb_{4-4z}Eu_{4z}W_8}$ (z = 0.00, 0.01, 0.02, 0.03, 0.04, 0.07, 0.10, 0.40, 0.70, 1.00) (Table S1e). Through the PL emission and decay lifetime measurements of the Eu^{3+}/Tb^{3+} codoped $\mathbf{Gd_4W_8}$ system, it can be found that in Eu^{3+}/Tb^{3+} codoped samples, Tb^{3+} ions can transfer energy to Eu^{3+} ions under excitation at 370 nm. When the molar concentration of Tb^{3+} ions is fixed as 0.9 and that of Eu^{3+} ions increases from 0.01 to 0.08, the intensity and decay lifetime of the emission peak at 545 nm continually declines and the ET efficiency increases from 7.9% for $\mathbf{Gd_{0.36}Tb_{3.6}Eu_{0.04}W_8}$ to 67.3% for $\mathbf{Gd_{0.08}Tb_{3.6}Eu_{0.32}W_8}$. In this system, the ET mechanism ($Tb^{3+} \rightarrow Eu^{3+}$) abides by the nonradiative dipole−dipole interaction. Under excitation at 370 nm, the color-tunable emissions of $\mathbf{Tb_{4-4z}Eu_{4z}W_8}$ (z = 0.00, 0.01, 0.02, 0.03, 0.04, 0.07, 0.10, 0.40, 0.70, 1.00) show visible green-, near-white-, orange-, and red-emitting lights. When codoping trace amounts of Eu^{3+} ions in $\mathbf{Tb_4W_8}$, under excitation at 370 nm, $\mathbf{Tb_{3.92}Eu_{0.08}W_8}$ displays near-white-light emission. Therefore, hetero-Ln substituted POM materials may have large potentials in the application of W-LEDs.

EXPERIMENTAL SECTION

Synthesis of $Na_{10}[Gd_2(C_2O_4)(H_2O)_4(OH)W_4O_{16}]_2{\cdot}30H_2O$ ($\mathbf{Gd_4W_8}$). $Na_2WO_4{\cdot}2H_2O$ (2.430 g, 7.37 mmol) and oxalic acid (0.063 g, 0.70 mmol) were dissolved in 20 mL of distilled water upon stirring, and the pH was regulated to 7.5 using 6.0 mol/L HCl. After the mixture was stirred for 20 min, $GdCl_3$ (0.250 g, 0.948 mmol) was added and another sustainable stirring for 0.5 h was needed. Eventually, the solution was placed in a 90 °C water bath for 2 h and then filtered (Figure 1a, b). Slow evaporation of the filtrate at ambient temperature for ca. 1 week resulted in colorless square lamellar crystals of $\mathbf{Gd_4W_8}$. Yield: 0.24 g (18.3% based on oxalic acid). Anal. calcd (%): H, 2.19; C, 1.28; Na, 6.15; W, 39.33; Gd, 16.82. Found: H, 2.00; C, 1.39; Na, 6.28; W, 39.11; Gd, 16.97.

Syntheses of Eu^{3+} and/or Tb^{3+} Codoped $\mathbf{Gd_4W_8}$ Materials. The syntheses of $\mathbf{Gd_{4-4a}Eu_{4a}W_8}$ (a = 0.01, 0.02, 0.03, 0.04, 0.07, 0.10, 0.40, 0.70, 1.00), $\mathbf{Gd_{4-4b}Tb_{4b}W_8}$ (b = 0.01, 0.02, 0.03, 0.04, 0.07, 0.10, 0.40, 0.70, 1.00), $\mathbf{Gd_{0.4-4x}Eu_{4x}Tb_{3.6}W_8}$ (x = 0.00, 0.01, 0.02, 0.03, 0.04, 0.05, 0.06, 0.07, 0.08), $\mathbf{Gd_{3.6-4y}Tb_{4y}Eu_{0.4}W_8}$ (y = 0.00, 0.10,

DOI: 10.1021/acs.inorgchem.9b02903
Inorg. Chem. 2020, 59, 648−660

0.20, 0.30, 0.40, 0.50, 0.60, 0.70, 0.80), and $Tb_{4-4z}Eu_{4z}W_8$ (z = 0.00, 0.01, 0.02, 0.03, 0.04, 0.07, 0.10, 0.40, 0.70, 1.00) were analogous to that of Gd_4W_8 except that $EuCl_3$, $GdCl_3$, and $TbCl_3$ replace $GdCl_3$ in the appropriate molar ratio (Figure 1c, Tables S1a–S1e). The theoretical and experimental mass percentages of W, Gd, Eu, and Tb ions in them were provided in Tables S1f–S1j.

RESULTS AND DISCUSSION

Structure Depiction. Crystallogaphical data of Gd_4W_8 are exhibited in Table S2. The molecular unit of Gd_4W_8 is composed of 1 double-oxalate-bridging tetra-Gd-substituted $[Gd_2(C_2O_4)(H_2O)_4(OH)W_4O_{16}]_2^{10-}$ (**Gd_4W_8-1**) polyoxoanion (POA), 10 Na^+ cations, and 30 lattice water molecules (Figure 2a). The dimeric **Gd_4W_8-1** POA is approximately 1.61 nm long and is constructed by two divacant Lindqvist $[W_4O_{16}]^{8-}$ ($\{W_4\}$) segments, four Gd^{3+} ions, and two oxalate ligands (Figure 2b). The divacant Lindqvist $\{W_4\}$ segments can be considered as a plenary Lindqvist $[W_6O_{19}]^{2-}$ segment losing two $\{WO_6\}$ octahedra (Figure 2c). Two $Gd1^{3+}$ centers simultaneously are embedded into the two vacancies of one divacant Lindqvist $\{W_4\}$ segment via six μ_2-O atoms and one μ_6-O atom, which results in one di-Gd-substituted Lindqvist $[Gd_2(H_2O)_4(OH)W_4O_{16}]^{3-}$ $\{Gd_2W_4\}$ fragment (Figure 2d). Two $\{Gd_2W_4\}$ fragments are connected by four carboxylic O atoms of two oxalate ligands, in other words, each $Gd1^{3+}$ center performs as a metal linker between $\{W_4\}$ segment and the oxalate ligand. Four $Gd1^{3+}$ centers together with two oxalate ligands exhibit a rectangle distribution; four $Gd1^{3+}$ centers are located on four vertexes of the rectangle, and two oxalate ligands occupy two sides of the rectangle (Figure S2a). In the simplified view of the rectangle formed by four Gd^{3+} centers, the distances between Gd^{3+} ions are 3.661–6.299 Å (Figure S2b). Four $Gd1^{3+}$ centers possess the same coordination environments and reveal the analogous monocapped square antiprismatic geometries (Figure 2e). Specifically, every $Gd1^{3+}$ center is surrounded by three μ_2-O atoms [Gd1–O1 2.202(9) Å, Gd1–O2 2.188(9) Å, Gd1–O9 2.458(8) Å] and one μ_6-O atom [Gd1–O4 2.852(8) Å] from one $\{W_4\}$ segment, two aqua ligands [Gd1–O1W 2.409(11) Å, Gd1–O2W 2.389(11) Å], two oxalate O atoms [Gd1–O10 2.427(11) Å, Gd1–O11 2.450(16) Å], and one hydroxyl O atom [Gd1–O12 1.912(5) Å]. Therefore, oxalate ligands play a role of organic linkers between two $\{Gd_2W_4\}$ fragments, which lead to the formation of dimeric **Gd_4W_8-1** POA.

It should be mentioned that two crystallographically independent Na^+ centers ($Na1^+$ and $Na2^+$) are seen in the structure, which exhibit diverse octahedral environments. The coordination sphere of the $Na1^+$ center is determined by a terminal O6 atom from one $\{W_4\}$ segment and five aqua ligands (i.e., O3W, O3WA, O4W, O5W, O6W), whereas the coordination sphere of the $Na2^+$ center is defined by two terminal O atoms (i.e., O3C, O3D) and four aqua ligands (i.e., O4W, O4WB, O7W, O7WB) (Figure S3a–b). $Na1^+$ and $Na2^+$ centers connect with each other through an aqua ligand (O4W), which leads to the dinuclear $[Na_2O_3(H_2O)_8]^{4-}$ cluster (Figure 3a). In addition, the dinuclear $[Na_2O_3(H_2O)_8]^{4-}$ cluster combines with a $Na1A^+$ center via the edge-sharing mode (O3W–O3WA), which leads to the formation of a trinuclear $[Na_3O_4(H_2O)_{11}]^{5-}$ cluster (Figure 3b). It is interesting that neighboring $[Na_3O_4(H_2O)_{11}]^{5-}$ clusters are interconnected to build a picturesque 1-D sinusoidal Na–O cluster chain (Figure 3c). It should be noted that this 1-D sinusoidal Na–O cluster chain is very unusual in inorganic chemistry. In the *ac* plane, neighboring 1-D sinusoidal Na–O cluster chains are aligned in the –ABAB– mode (Figure S3c) when taking no account of **Gd_4W_8-1** POAs. In the *ab* plane, neighboring 1-D sinusoidal Na–O cluster chains also show the –ABAB– alignment mode (Figure S3d). The most striking

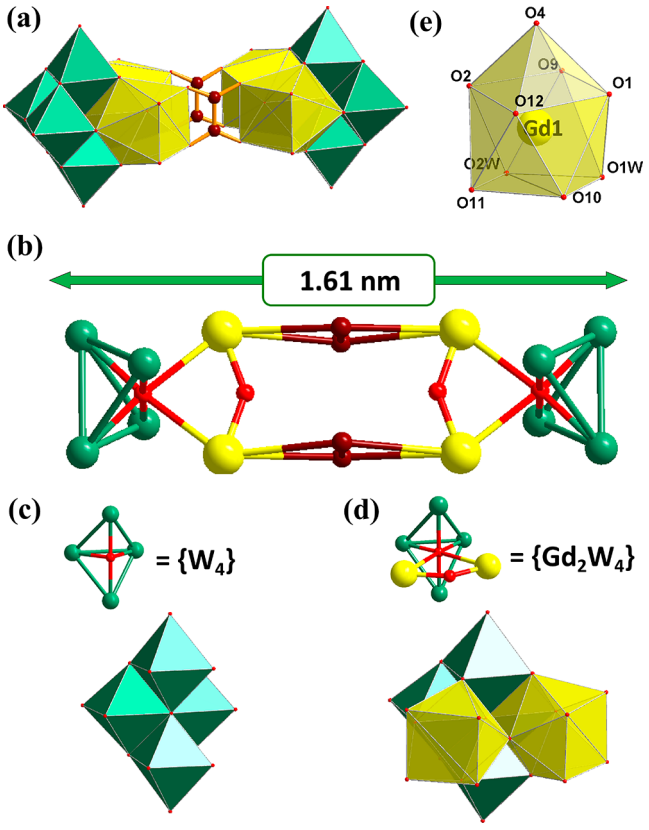

Figure 2. (a) The dimeric **Gd_4W_8-1** POA. (b) Simplified ball-and-stick view of **Gd_4W_8-1**. (c) View of the $\{W_4\}$ segment. (d) View of the $\{Gd_2W_4\}$ group. (e) Monocapped square antiprismatic configuration of the $Gd1^{3+}$ ion. Code: $\{WO_6\}$, bottle green octahedra; O, rose red spheres; W, bottle green spheres; Gd, bright yellow spheres; C, brown spheres.

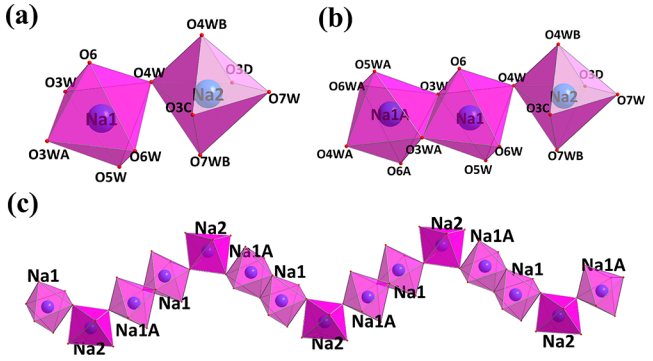

Figure 3. (a) The dinuclear $[Na_2O_3(H_2O)_8]^{4-}$ cluster formed by a $Na1^+$ and a $Na2^+$ center via an aqua ligand. (b) The trinuclear $[Na_3O_4(H_2O)_{11}]^{5-}$ clusters formed by a dinuclear $[Na_2O_3(H_2O)_8]^{4-}$ cluster connecting a $Na1^+A$ center in the edge-sharing mode. (c) The sinusoidal Na–O cluster chain constructed from $[Na_3O_4(H_2O)_{11}]^{5-}$ clusters. Na, violet spheres. Symmetry code: A: $-0.5 - x, 0.5 - y, -z$; B: $-x, y, 1 - z$; C: $0.5 - x, y, 1 - z$; D: $-0.5 + x, 0.5 - y, z$.

DOI: 10.1021/acs.inorgchem.9b02903
Inorg. Chem. 2020, 59, 648–660

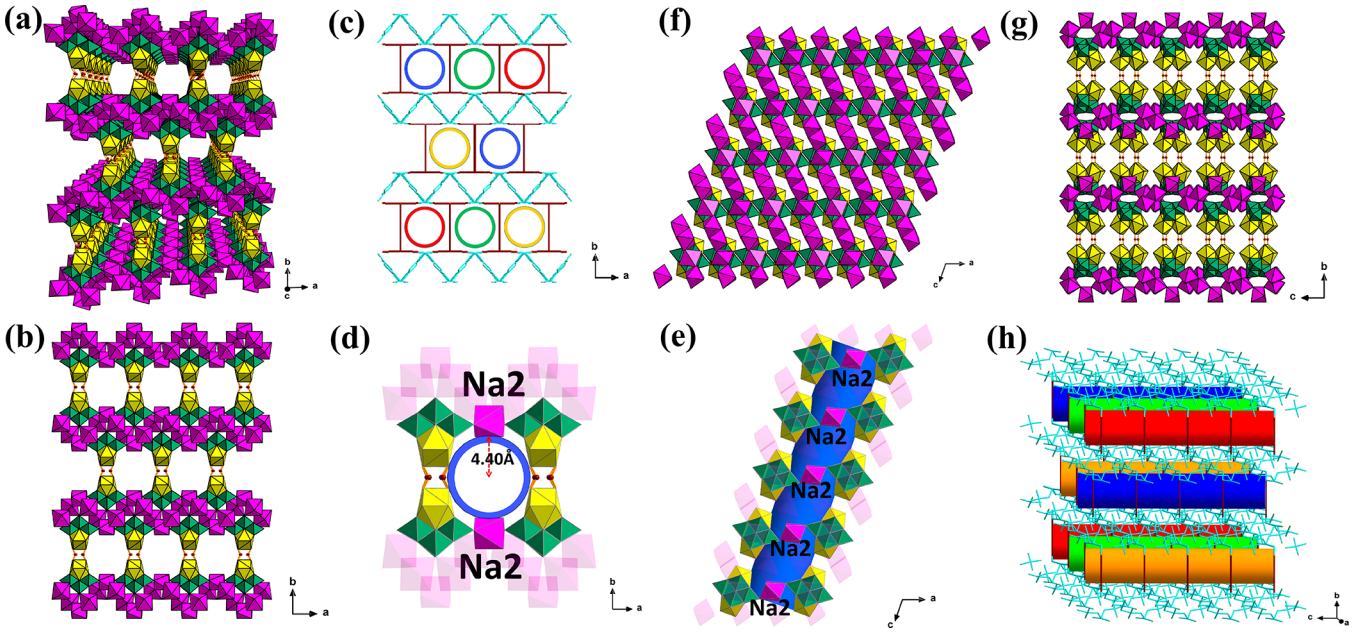

Figure 4. (a) The intriguing 3-D extended porous framework. (b) The 3-D porous framework viewed along the *c* axis. (c) The simplified 3-D porous framework viewed along the *c* axis. (d) The combination between two $[Gd_2(C_2O_4)(H_2O)_4(OH)W_4O_{16}]_2^{10-}$ polyoxoanions and two $Na2^+$ centers through four O/H_2O linkers. (e) The 1-D channels constructed from $[Gd_2(C_2O_4)(H_2O)_4(OH)W_4O_{16}]_2^{10-}$ polyoxoanions and $Na2^+$ centers. (f) The 3-D porous framework viewed along the *b* axis. (g) The 3-D porous framework viewed along the *a* axis. (h) Simplified 3-D porous framework showing the multichannel structure.

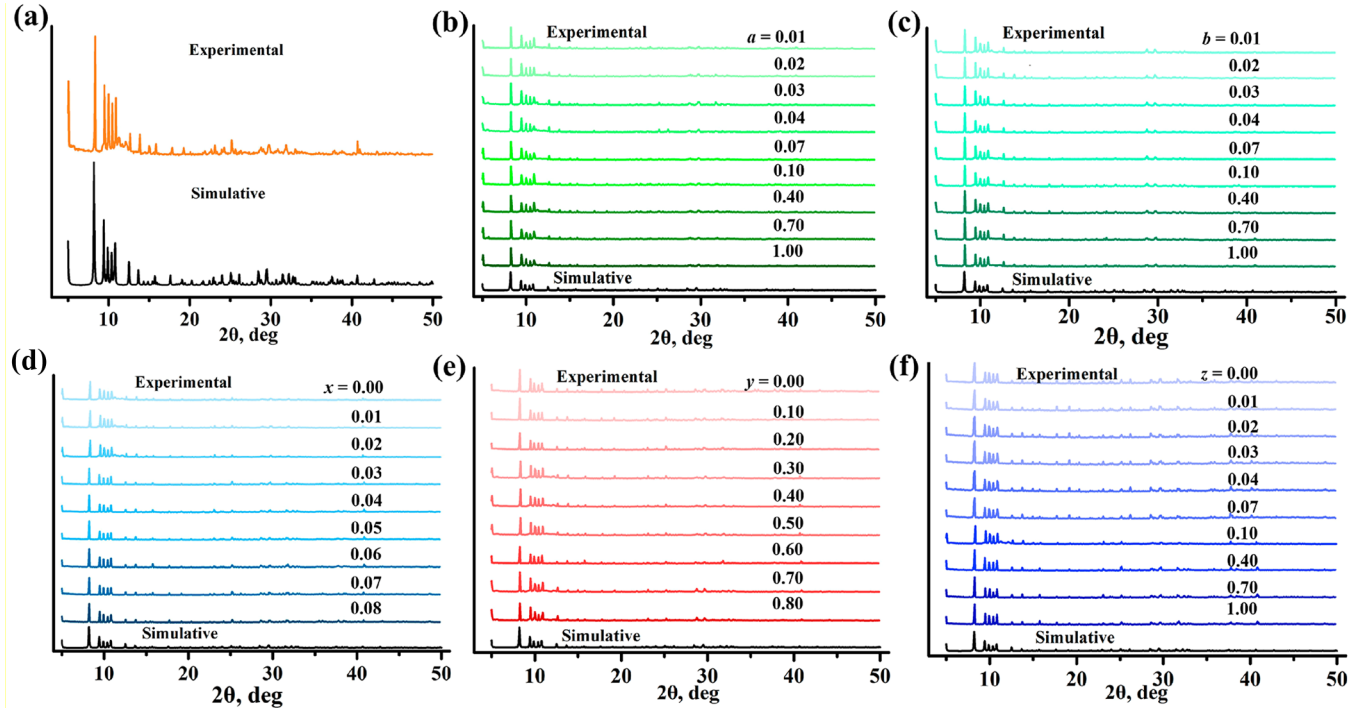

Figure 5. (a) Experimental and simulative PXRD patterns of Gd_4W_8. (b–f) Comparisons of experimental PXRD patterns of $Gd_{4-4a}Eu_{4a}W_8$ (a = 0.01, 0.02, 0.03, 0.04, 0.07, 0.10, 0.40, 0.70, 1.00), $Gd_{4-4b}Tb_{4b}W_8$ (b = 0.01, 0.02, 0.03, 0.04, 0.07, 0.10, 0.40, 0.70, 1.00), $Gd_{0.4-4x}Eu_{4x}Tb_{3.6}W_8$ (x = 0.00, 0.01, 0.02, 0.03, 0.04, 0.05, 0.06, 0.07, 0.08), $Gd_{3.6-4y}Tb_{4y}Eu_{0.4}W_8$ (y = 0.00, 0.10, 0.20, 0.30, 0.40, 0.50, 0.60, 0.70, 0.80), and $Tb_{4-4z}Eu_{4z}W_8$ (z = 0.00, 0.01, 0.02, 0.03, 0.04, 0.07,0.10, 0.40, 0.70, 1.00) and simulative PXRD pattern of Gd_4W_8.

feature is that 1-D sinusoidal Na–O cluster chains connect Gd_4W_8-**1** POAs together, giving rise to an attractive 3-D porous framework (Figure 4a). Viewed along the *c* axis, Gd_4W_8-**1** POAs as pillars link the up–down neighboring 1-D sinusoidal Na–O cluster chains (Figure 4b, c). In the 3-D extended porous framework, every two Gd_4W_8-**1** POAs are joined by two $Na2^+$ centers through four O/H_2O linkers, which generates the 1-D channels with the radius of about 4.40 Å (Figure 4d, e). These 1-D channels somewhat resemble pipelines and are parallel to the *c* axis (Figure 4e–h, Figure S4). Lattice water molecules are filled in these channels.

DOI: 10.1021/acs.inorgchem.9b02903
Inorg. Chem. 2020, 59, 648–660

IR Spectra and PXRD Patterns. Because the radii of Gd^{3+}, Eu^{3+}, and Tb^{3+} ions are close (Table S2) and the structure of $\mathbf{Gd_4W_8}$ is the same to those of our previously reported Ln-IPOTIOHMs $Na_{10}[Eu_2(C_2O_4)(H_2O)_4(OH)W_4O_{16}]_2{\cdot}30H_2O$ ($\mathbf{Eu_4W_8}$) and $Na_{10}[Tb_2(C_2O_4)(H_2O)_4(OH)W_4O_{16}]_2{\cdot}30H_2O$ ($\mathbf{Tb_4W_8}$),[55] Eu^{3+} and Tb^{3+} ions can be easily codoped into the host of $\mathbf{Gd_4W_8}$. To prove the structural consistence of $\mathbf{Gd_{4-4a}Eu_{4a}W_8}$ (a = 0.01, 0.02, 0.03, 0.04, 0.07, 0.10, 0.40, 0.70, 1.00), $\mathbf{Gd_{4-4b}Tb_{4b}W_8}$ (b = 0.01, 0.02, 0.03, 0.04, 0.07, 0.10, 0.40, 0.70, 1.00), $\mathbf{Gd_{0.4-4x}Eu_{4x}Tb_{3.6}W_8}$ (x = 0.00, 0.01, 0.02, 0.03, 0.04, 0.05, 0.06, 0.07, 0.08), $\mathbf{Gd_{3.6-4y}Tb_{4y}Eu_{0.4}W_8}$ (y = 0.00, 0.10, 0.20, 0.30, 0.40, 0.50, 0.60, 0.70, 0.80), and $\mathbf{Tb_{4-4z}Eu_{4z}W_8}$ (z = 0.00, 0.01, 0.02, 0.03, 0.04, 0.07, 0.10, 0.40, 0.70, 1.00), their IR spectra and PXRD patterns were collected. Their IR spectra are identical (Figure S5a–f). Therein, the IR spectrum in the low wavenumber region of ca. 400–1000 cm^{-1} of $\mathbf{Gd_4W_8}$ demonstrates that the three strong absorption peaks at 689, 842, and 949 cm^{-1} originate severally from the stretching vibrations of corner-sharing W–O_b–W, edge-sharing W–O_c–W, and terminal W–O_t bands of vacant $[W_4O_{16}]^{8-}$ units.[56] In the middle range of ca. 1000–2000 cm^{-1}, a weak absorption peak at 1328 cm^{-1} can be viewed as the symmetric stretching vibration of carboxylate groups (CO_2^-) of oxalate ligands, while a strong peak at 1662 cm^{-1} is assigned to the common interaction of the O–H bending vibration of H_2O molecules and the asymmetric stretching vibration of carboxylate groups of oxalate ligands.[57,58] In the high wavenumber region of ca. 2000–4000 cm^{-1}, a wide absorption band at ca. 3300–3500 cm^{-1} stems from the O–H stretching vibration of H_2O molecules. The absorption band of the Gd–O band cannot be found, probably on account of dominating ionic interactions between vacant $[W_4O_{16}]^{8-}$ units and Gd^{3+} ions.[59−62] Their PXRD patterns are also well-matched with the single-crystal XRD pattern of $\mathbf{Gd_4W_8}$ (Figure 5a–f). Thus, all used samples for measurements are all isostructural and pure.

Photoluminescence (PL). With respect to various Ln^{3+} codoped light-emitting materials, recently, their functional applications in W-LEDs, luminescent thermometers, and temperature-dependent imaging reagents are receiving intimate attention.[63−65] The comprehensive PL behaviors of various Ln^{3+} codoped light-emitting materials principally stem from the common results of multiple factors, such as simultaneous emissions of various Ln luminescent centers, ET process between different Ln centers, the concentration of Ln luminescent centers, the concentration quenching, and so forth.[66,67] Therein, Eu^{3+} and Tb^{3+} ions are respectively red and green components, which can be codoped into the same host with an appropriate concentration ratio to stimulate the study of PL behaviors of various Ln^{3+} (Ln^{3+} = Eu^{3+}, Gd^{3+}, Tb^{3+}) codoped POM materials. It is essential to explore systematically the ET process and color-tunable property through various Ln^{3+} codoped POM materials. The intramolecular ET from the donor to the acceptor can be determined through the following rules: (i) the overlap of emission peaks of the donor with excitation peaks of the acceptor; (ii) the increase of emission intensity or decay time of the acceptor; and (iii) the decrease of emission intensity or decay time of the donor.[68,69] Herein, various $\mathbf{Gd_{4-4a}Eu_{4a}W_8}$ (a = 0.01, 0.02, 0.03, 0.04, 0.07, 0.10, 0.40, 0.70, 1.00), $\mathbf{Gd_{4-4b}Tb_{4b}W_8}$ (b = 0.01, 0.02, 0.03, 0.04, 0.07, 0.10, 0.40, 0.70, 1.00), $\mathbf{Gd_{0.4-4x}Eu_{4x}Tb_{3.6}W_8}$ (x = 0.00, 0.01, 0.02, 0.03, 0.04, 0.05, 0.06, 0.07, 0.08), $\mathbf{Gd_{3.6-4y}Tb_{4y}Eu_{0.4}W_8}$ (y = 0.00, 0.10, 0.20, 0.30, 0.40, 0.50, 0.60, 0.70, 0.80), and $\mathbf{Tb_{4-4z}Eu_{4z}W_8}$ (z = 0.00, 0.01, 0.02, 0.03, 0.04, 0.07, 0.10, 0.40, 0.70, 1.00) samples were prepared, and emission spectra and decay times as testing methods were utilized to analyze ET between Eu^{3+} and Tb^{3+} ions and the color-tunable property. The room-temperature excitation and emission spectrograms of $\mathbf{Gd_{1.2}Eu_{2.8}W_8}$ and $\mathbf{Gd_{1.2}Tb_{2.8}W_8}$ were measured (Figure 6a, b). As shown in Figure 6a, the

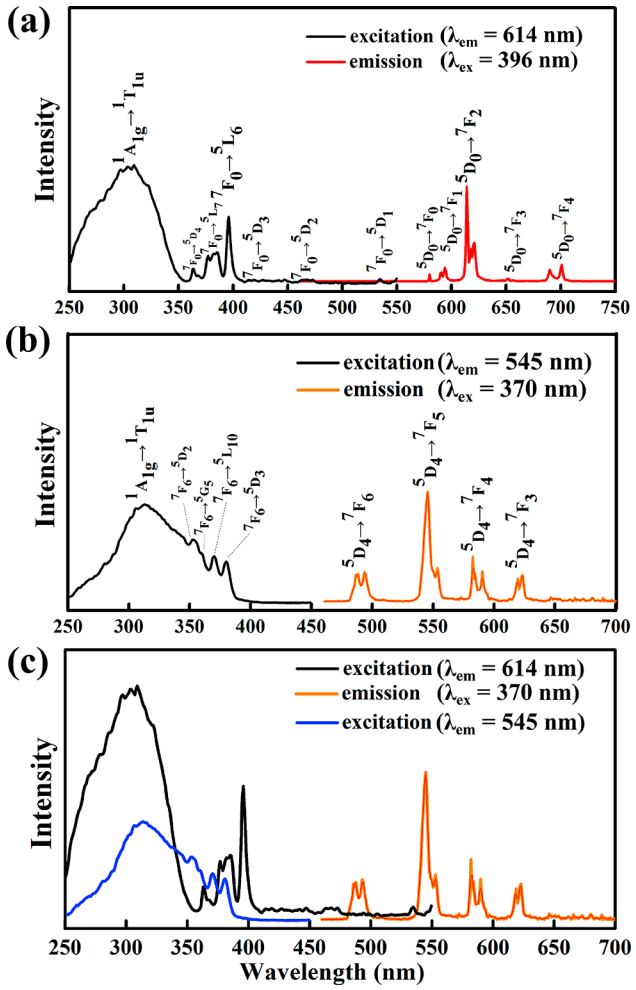

Figure 6. (a) Emission spectrogram upon λ_{ex} = 396 nm and excitation spectrogram by supervising the peak at λ_{em} = 614 nm of $\mathbf{Gd_{1.2}Eu_{2.8}W_8}$. (b) Emission spectrogram upon λ_{ex} = 370 nm and excitation spectrogram by supervising the peak at λ_{em} = 545 nm of $\mathbf{Gd_{1.2}Tb_{2.8}W_8}$. (c) The emission spectrum of $\mathbf{Gd_{1.2}Tb_{2.8}W_8}$ (red), the excitation spectrum of $\mathbf{Gd_{1.2}Eu_{2.8}W_8}$ (black), and the excitation spectrum of $\mathbf{Gd_{1.2}Tb_{2.8}W_8}$ (blue).

excitation spectrogram (the black line) of $\mathbf{Gd_{1.2}Eu_{2.8}W_8}$ collected through supervising the strongest emission at 614 nm gives a wide excitation band centered at 310 nm derived from the $^1A_{1g}\rightarrow{}^1T_{1u}$ transition of O → W LMCT of $[W_4O_{16}]^{8-}$ segments and five excitation peaks at 364, 382, 396, 416, 464, and 535 nm that are respectively ascribed to Eu^{3+} $^7F_0\rightarrow{}^5D_4$, $^7F_0\rightarrow{}^5L_7$, $^7F_0\rightarrow{}^5L_6$, $^7F_0\rightarrow{}^5D_3$, $^7F_0\rightarrow{}^5D_2$, and $^7F_0\rightarrow{}^5D_1$ transitions,[70] where the Eu^{3+} strongest excitation peak is at 396 nm. Upon excitation at 396 nm, the emission spectrum (the red line) of $\mathbf{Gd_{1.2}Eu_{2.8}W_8}$ displays five prominent f–f emitting peaks at 580, 594, 614, 652, and 701 nm that are assigned to Eu^{3+} $^5D_0\rightarrow{}^7F_J$ (J = 0, 1, 2, 3, 4) transitions.[70] As revealed in Figure 6b, the excitation spectrum

DOI: 10.1021/acs.inorgchem.9b02903
Inorg. Chem. 2020, 59, 648–660

(the black line) of $Gd_{1.2}Tb_{2.8}W_8$ exhibits one broad excitation band at ca. 310 nm from the $^1A_{1g} \rightarrow {}^1T_{1u}$ transition of O → W LMCT of $[W_4O_{16}]^{8-}$ segments and four Tb^{3+} excitation peaks at 351 ($^7F_6 \rightarrow {}^5D_2$), 360 ($^7F_6 \rightarrow {}^5G_5$), 370 ($^7F_6 \rightarrow {}^5L_{10}$), and 377 ($^7F_6 \rightarrow {}^5D_3$) nm.[70−73] Under excitation at 370 nm of Tb^{3+} ions, the emission spectrogram of $Gd_{1.2}Tb_{2.8}W_8$ (the orange line) mainly reveals four *f*−*f* emission peaks at 493, 545, 582, and 623 nm originating from $Tb^{3+} {}^5D_4 \rightarrow {}^7F_J$ (J = 6, 5, 4, 3) transitions.[72,73] It is notable that a partial overlap between the $^5D_4 \rightarrow {}^7F_5$ emission peak at 545 nm of $Gd_{1.2}Tb_{2.8}W_8$ and the $^7F_0 \rightarrow {}^5D_1$ excitation peak at 535 nm of $Gd_{1.2}Eu_{2.8}W_8$ and an obvious excitation spectral overlap of $Gd_{1.2}Tb_{2.8}W_8$ and $Gd_{1.2}Eu_{2.8}W_8$ in the range of 374−390 nm can be observed (Figure 6c, Figure S6a), which indicate that the ET from the $^5D_4$ state of Tb^{3+} ions to the $^5D_1$ state of Eu^{3+} ions can happen.[53,74]

Furthermore, various Eu^{3+}-doped $Gd_{4-4a}Eu_{4a}W_8$ (a = 0.01, 0.02, 0.03, 0.04, 0.07, 0.10, 0.40, 0.70, 1.00) samples and various Tb^{3+}-doped $Gd_{4-4b}Tb_{4b}W_8$ (b = 0.01, 0.02, 0.03, 0.04, 0.07, 0.10, 0.40, 0.70, 1.00) samples were prepared to understand the relationship between luminescence intensity and concentration of Eu^{3+} and Tb^{3+} ions. Upon excitation at 396 nm of Eu^{3+} ions, the emission spectra of $Gd_{4-4a}Eu_{4a}W_8$ reveal that the emission intensity at 614 nm grows rapidly with increasing the concentration of Eu^{3+} ions in the range of 0.01−0.10 and then increases slowly with increasing the concentration of Eu^{3+} ions in the range of 0.10−1.00, which may be due to the slight concentration quenching (Figure 7a). The cross relaxation among adjacent Eu^{3+} ions is responsible for the concentration quenching of Eu^{3+} emission.[75−79] Under excitation at 370 nm of Tb^{3+} ions, the emission spectra of $Gd_{4-4b}Tb_{4b}W_8$ illustrate that the emission intensity at 545 nm ascends with the rising concentration of Tb^{3+} ions (Figure 7b). Therefore, the Eu^{3+} and Tb^{3+}-codoped $Gd_{0.4-4x}Eu_{4x}Tb_{3.6}W_8$ (x = 0.00−0.08) and $Gd_{3.6-4y}Tb_{4y}Eu_{0.4}W_8$ (y = 0.00−0.80) samples have been prepared for the investigation of ET between Eu^{3+} and Tb^{3+} ions. Therein, the concentration quenching of Eu^{3+} ions can be avoided effectively.

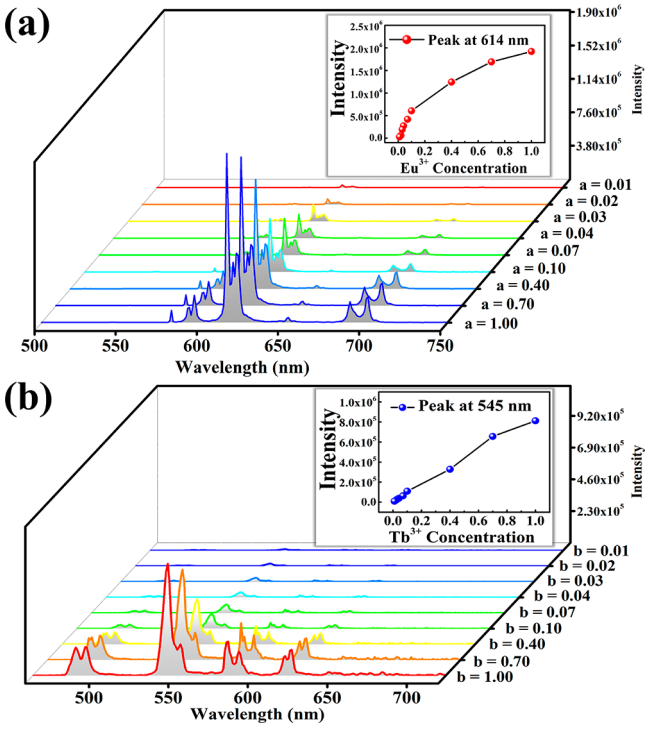

Figure 7. (a) Evolution of PL emitting spectra of $Gd_{4-4a}Eu_{4a}W_8$ with increasing the concentration of Eu^{3+} ions upon λ_{ex} = 396 nm. Inset is the variation of the emission peak intensity at 614 nm with increasing the concentration of Eu^{3+} ions. (b) Evolution of PL emitting spectra of $Gd_{4-4b}Tb_{4b}W_8$ with increasing the concentration of Tb^{3+} ions upon λ_{ex} = 370 nm. Inset is the variation of emission peak intensity at 545 nm with increasing the concentration of Tb^{3+} ions.

To better explore the ET mechanism between Tb^{3+} and Eu^{3+} ions, under the $^7F_6 \rightarrow {}^5L_{10}$ photoexcitation at 370 nm of Tb^{3+} ions, a series of decay time curves of the $^5D_4 \rightarrow {}^7F_5$ emission peak at 545 nm of Tb^{3+} ions for $Gd_{0.4-4x}Eu_{4x}Tb_{3.6}W_8$ were measured (Figure 8a) and can be simulated by the monoexponential function. As displayed in Figure 8a and b and Table S3, as the concentration of Eu^{3+} ions increases from 0 to 0.08, the PL lifetime of the emission peak at 545 nm significantly decreases from 642.86 to 210.18 μs, which is caused by ET from Tb^{3+} to Eu^{3+} ions. These decay lifetime curves conform to the monoexponential behavior, which indicates that the emission peak at 545 nm is primarily caused by the contribution of Tb^{3+} ions. Also, a series of decay lifetime curves of the $^5D_0 \rightarrow {}^7F_2$ emission peak at 614 nm of Eu^{3+} ions for $Gd_{0.4-4x}Eu_{4x}Tb_{3.6}W_8$ were measured and exhibit the double-exponential behavior (Figure S6b, Table S4). Therein, the short lifetime τ_1 and long lifetime τ_2 gradually increase as the concentration of Eu^{3+} ions increases, and two lifetimes may be caused by the common contribution of Eu^{3+} and Tb^{3+} ions. The above-mentioned analysis can be supported by the observation that because of ET from Tb^{3+} donors to Eu^{3+} acceptors, the decay lifetime of the emission peak at 545 nm (the $^5D_4 \rightarrow {}^7F_5$ transition of Tb^{3+} ions) decreases and the decay lifetime of the emission peak at 614 nm (the $^5D_0 \rightarrow {}^7F_2$ transition of Eu^{3+} ions) increases.

Because the molar concentration of Tb^{3+} ions is fixed as 0.90 and the concentration of Eu^{3+} ions varies from 0 to 0.08, the ET efficiency (η_{ET}) from Tb^{3+} to Eu^{3+} ions can be calculated by eq 1:[80−82]

$$\eta_{ET} = 1 - \tau_S/\tau_{S0} \quad (1)$$

In this equation, τ_S and τ_{S0} are the decay lifetimes of the emission peak at 545 nm ascribed to the Tb^{3+} $^5D_4 \rightarrow {}^7F_5$ transition (donors) with and without Eu^{3+} ions (acceptors). The η_{ET} values in $Gd_{0.4-4x}Eu_{4x}Tb_{3.6}W_8$ (x = 0.01−0.08) are 7.9%, 15.3%, 22.8%, 45.3%, 51.1%, 56.3%, 62.4%, and 67.3%, respectively (Figure 8c). Simultaneously, the emission spectra of $Gd_{0.4-4x}Eu_{4x}Tb_{3.6}W_8$ (x = 0.01−0.08) measured upon excitation at 370 nm simultaneously exhibit emissions of Eu^{3+} and Tb^{3+} ions (Figure 8d), where the peaks at 580, 594, 614, 652, and 701 nm are attributable to $Eu^{3+} {}^5D_0 \rightarrow {}^7F_J$ (J = 0, 1, 2, 3, 4) transitions and the peaks at 493, 545, 582, and 623 nm are assigned to the Tb^{3+} $^5D_4 \rightarrow {}^7F_J$ (J = 6, 5, 4 and 3) transitions. As shown in Figure 8d, with increasing the concentration of Eu^{3+} ions in $Gd_{0.4-4x}Eu_{4x}Tb_{3.6}W_8$ (x = 0.01−0.08), the emission intensity gradually declines for the peak at 545 nm (the $^5D_4 \rightarrow {}^7F_5$ transition of Tb^{3+} ions) but grows for the peak at 614 nm (the $^5D_0 \rightarrow {}^7F_2$ transition of Eu^{3+} ions), which indicates that the increase of concentration of Eu^{3+} ions will singly result in the successive enhancement of luminescence quenching to Tb^{3+} ions.

Many cases have been shown as examples that luminescence quenching can be owed to ET from donors to acceptors when acceptors appear in the lattice.[83] Blasse proposed that the

DOI: 10.1021/acs.inorgchem.9b02903
Inorg. Chem. 2020, 59, 648−660

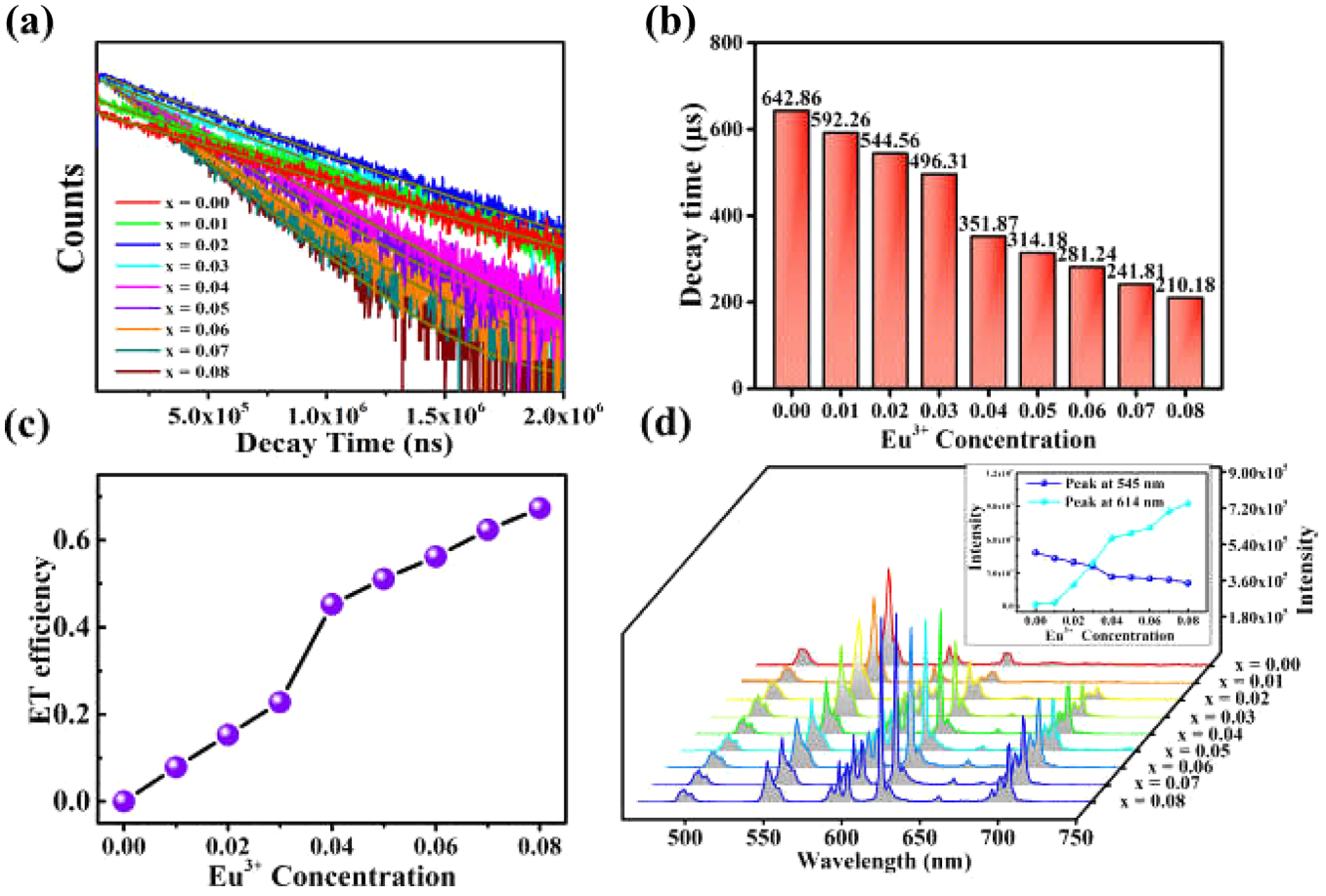

Figure 8. (a) Decay lifetime curves of the peak at 545 nm for $\mathbf{Gd_{0.4-4x}Eu_{4x}Tb_{3.6}W_8}$ (x = 0.00−0.08) upon λ_{ex} = 370 nm. (b) PL lifetimes of the peak at 545 nm for $\mathbf{Gd_{0.4-4x}Eu_{4x}Tb_{3.6}W_8}$ (x = 0.00−0.08) upon λ_{ex} = 370 nm. (c) Dependence of ET efficiency ($Tb^{3+} \rightarrow Eu^{3+}$) on concentration of Eu^{3+} ions upon λ_{ex} = 370 nm for $\mathbf{Gd_{0.4-4x}Eu_{4x}Tb_{3.6}W_8}$. (d) Emission spectra of $\mathbf{Gd_{0.4-4x}Eu_{4x}Tb_{3.6}W_8}$ (x = 0.00−0.08) obtained upon λ_{ex} = 370 nm.

critical distance (R_c) of ET from donors to acceptors can be calculated by eq 2:[84,85]

$$R_c = 2 \times [3V/(4\pi\chi_c Z)]^{1/3} \quad (2)$$

where V represents the volume of a unit cell, χ_c (critical concentration) is the total molar concentration of the donor (Tb^{3+}) and the acceptor (Eu^{3+}) in a unit cell when the emission intensity of donor (Tb^{3+}) is half of that in the absence of the acceptor (Eu^{3+}), and Z stands for the number of the donor (Tb^{3+}) in the host. In the Tb^{3+} single-doped host, V = 3943.3 Å^3 and Z = 8 (Figure S7).[55] R_c is calculated to be 9.93 Å for χ_c = 0.9628 (determined from Figure S6c). Therefore, the electric multipolar interactions can be viewed as the dominating ET mechanism from Tb^{3+} to Eu^{3+} ions because R_c > 5.0 Å is the precondition of electric multipolar interaction and R_c < 5.0 Å is the precondition of exchange interaction.[86−89] On the basis of Dexter's expression and Reisfeld's approximation,[86−89] the electric multipolar interactions are divided into the dipole−dipole interaction, the dipole−quadrupole interaction, and the quadrupole−quadrupole interaction. The electric multipolar interactions can be determined through eq 3:

$$\eta_{S0}/\eta_S \propto C^{n/3} \quad (3)$$

In eq 3, C is the total molar concentration of Tb^{3+} and Eu^{3+} ions. The values of n = 6, 8, and 10 represent, respectively, dipole−dipole, dipole−quadrupole, and quadrupole−quadrupole interactions. The values for η_{S0} and η_S represent luminous quantum efficiencies of the host (Tb^{3+}) ions in the absence and presence of Eu^{3+} ions, respectively, and η_{S0}/η_S can be replaced by I_{S0}/I_S to some degree (Figure 8d). I_{S0} and I_S respectively are the emission intensities of the peak at 545 nm (the $^5D_4 \rightarrow {}^7F_5$ transition of Tb^{3+} ions) in the absence and presence of Eu^{3+} ions for $\mathbf{Gd_{0.4-4x}Eu_{4x}Tb_{3.6}W_8}$. Thus, we can determine the ET mechanism from Tb^{3+} to Eu^{3+} ions by eq 4:

$$I_{S0}/I_S \propto C^{n/3} \quad (4)$$

As shown in Figure 9a−c, the linear relationships between I_{S0}/I_S and $C^{n/3}$ can be fitted considering that n is equal to 6, 8, and 10, respectively, which afforded the agreement factor R^2 values that are 0.91741 (n = 6), 0.91608 (n = 8), and 0.9145 (n = 10). It can be observed that the best linear fitting can be obtained (R^2 = 0.91741) when n is equal to 6; therefore, the multipolar ET mechanism from Tb^{3+} to Eu^{3+} ions is a nonradiative dipole−dipole interaction.

The schematic energy level diagram interpreting ET from Tb^{3+} to Eu^{3+} ions is presented in Figure 10. Upon excitation at 370 nm, by absorbing ultraviolet−visible radiation, electrons at the ground state ($^7F_6$) of Tb^{3+} ions jump to the $^5L_{10}$ state and decline to the $^5D_4$ state in form of nonradiative relaxation. Afterward, partial emission energy at the $^5D_4$ state leads to the $^5D_4 \rightarrow {}^7F_J$ (J = 6, 5, 4, and 3) emission transitions of Tb^{3+} ions, and the energy partially migrates to the $^5D_1$ state of Eu^{3+} ions due to the matched energy gap between $^5D_4 \rightarrow {}^7F_5$ (18.35 ×

DOI: 10.1021/acs.inorgchem.9b02903
Inorg. Chem. 2020, 59, 648−660

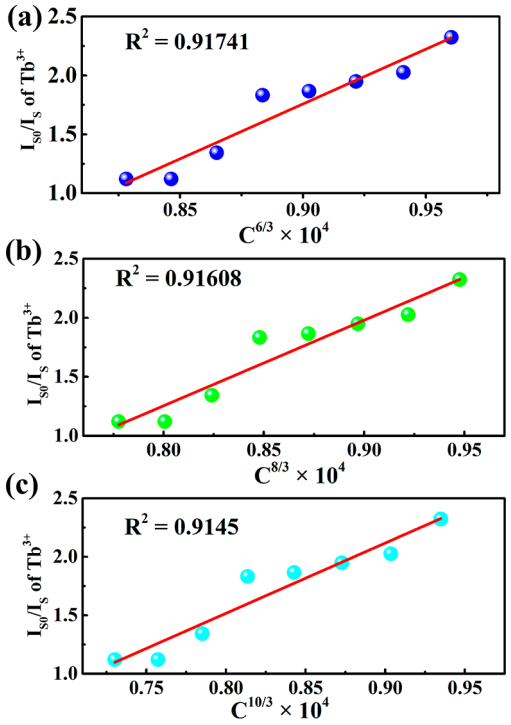

Figure 9. (a–c) Dependence of I_{S0}/I_0 of the $^5D_4 \rightarrow {}^7F_5$ transition from Tb^{3+} ions on $C^{6/3}$, $C^{8/3}$, and $C^{10/3}$.

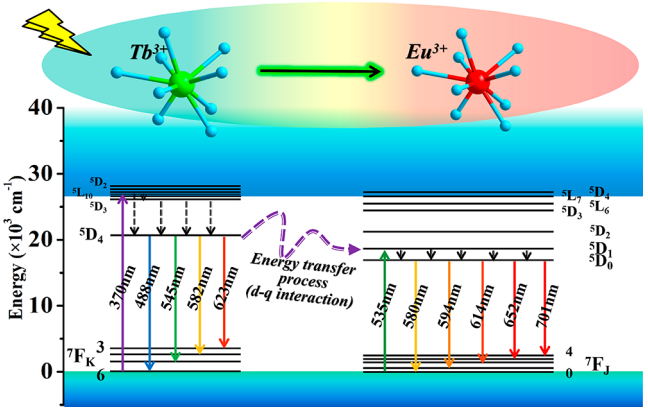

Figure 10. Schematic energy level diagram indicating the ET process from Tb^{3+} ions to Eu^{3+} ions corresponding to dipole–dipole interaction. The solid line is radiation transition and the dotted line is nonradiative transition.

10^3 cm^{-1}) of Tb^{3+} ions and $^7F_0 \rightarrow {}^5D_1$ (18.69×10^3 cm^{-1}) transitions of Eu^{3+} ions (Table S5). At the moment, photons at the $^5D_1$ state of Eu^{3+} ions drop to the $^5D_0$ state and give out radiant $^5D_0 \rightarrow {}^7F_J$ (J = 0, 1, 2, 3, 4) transitions.[70]

To deduce whether ET from Eu^{3+} to Tb^{3+} ions occurs, upon excitation at 396 nm of Eu^{3+} ions, the emitting spectra of $\mathbf{Gd_{0.4-4x}Eu_{4x}Tb_{3.6}W_8}$ (x = 0.01–0.08) give out only strong emission peaks of Eu^{3+} ions at 580, 594, 614, 652, and 701 nm ascribed to $Eu^{3+5}D_0 \rightarrow {}^7F_J$ (J = 0, 1, 2, 3, 4) transitions, and the emission peak intensity at 614 nm grows considerably as the concentration of Eu^{3+} ions increases (Figure S8a and S8b), which indicates that ET from Eu^{3+} to Tb^{3+} ions does not occur upon excitation at 396 nm. In addition, $\mathbf{Gd_{3.6-4y}Tb_{4y}Eu_{0.4}W_8}$ (y = 0–0.80) were also prepared to affirm that Tb^{3+} ions can transfer energy uniaxially to Eu^{3+} ions. When exciting $\mathbf{Gd_{3.6-4y}Tb_{4y}Eu_{0.4}W_8}$ (y = 0–0.80) using a light of 370 nm, their emitting spectra simultaneously generate emissions of Eu^{3+} and Tb^{3+} ions (Figure S9a and S9b), in which the peaks at 580, 594, 614, 652, and 701 nm originate from $Eu^{3+5}D_0 \rightarrow {}^7F_J$ (J = 0, 1, 2, 3, 4) transitions of ions and the peaks at 493, 545, 582, and 623 nm are derived from $Tb^{3+5}D_4 \rightarrow {}^7F_J$ (J = 6, 5, 4, 3) transitions. As the Tb^{3+} concentration increases, the emitting peak intensity at 614 nm is gradually enhanced, which can also be attributable to ET from Tb^{3+} to Eu^{3+} ions. It implies that the ratio of emission intensity between Eu^{3+} and Tb^{3+} ions can be adjusted through tuning the molar concentration proportion of Eu^{3+} and Tb^{3+} ions and further to shift the emission color of the Eu^{3+}/Tb^{3+} codoped samples.

The CIE diagram 1931 is an effective method to certify the color authenticity. The chromaticity coordinates, dominant wavelength, color purity, and CCT are important optic parameters. Therein, chromaticity coordinates can represent the accurate emission colors of luminescent materials, and the color based on dominant wavelength is agreement with that of a luminescent material in theory. Color purity is usually employed to demonstrate the brightness of colors, which can be calculated by eq 5:

$$\text{color purity} = [(x - x_i)^2 + (y - y_i)^2/(x_d - x_i)^2 + (y_d - y_i)^2]^{1/2} \quad (5)$$

where (x, y) is the color coordinate of the light source, (x_d, y_d) is the coordinate involving the dominant wavelength, and (x_i, y_i) is the coordinate of the white light at (0.3333, 0.3333).

The light sources with different CCTs can give rise to different subjective feelings to people. The feeling from light is warm when CCT is lower than 3000 K, standard in the range of 3000–5000 K, and cold when it is higher than 5000 K. CCT can be calculated by the eq 6:

$$\text{CCT} = 499.0n^3 + 3525.0n^2 + 6823.3n + 5520.22 \quad (6)$$

$$n = (x - x_e)/(y_e - y)$$

where (x_e, y_e) is the epicenter coordinate (0.3320, 0.1858).[90−95]

Due to the existence of ET from Tb^{3+} to Eu^{3+} ions, under excitation at 370 nm, the simultaneous emissions of Eu^{3+} and Tb^{3+} ions will support the investigation of color-tunable emission property. To better observe the emission color shift, the emission spectra, CIE 1931 diagram and luminous photographs of $\mathbf{Tb_{4-4z}Eu_{4z}W_8}$ (z = 0.00, 0.01, 0.02, 0.03, 0.04, 0.07, 0.10, 0.40, 0.70, 1.00) were collected under excitation at 370 nm. Upon excitation at 370 nm, emission spectra of $\mathbf{Tb_{4-4z}Eu_{4z}W_8}$ also show simultaneous emissions of Eu^{3+} and Tb^{3+} ions (Figure 11a). As the molar concentration of Eu^{3+} ions increases and that of Tb^{3+} ions decreases, the emission intensity at 545 nm gradually weakens and the emission intensity at 614 nm of Eu^{3+}ions enhances (Figure 11b, c). It can be explicitly seen that their CIE color coordinates of $\mathbf{Tb_{4-4z}Eu_{4z}W_8}$ (z = 0.00, 0.01, 0.02, 0.03, 0.04, 0.07, 0.10, 0.40, 0.70, 1.00) could be indexed from (0.332, 0.531) to (0.652, 0.343) with the growing molar concentration of Eu^{3+} ions from 0 to 1.0 (Table S6). The relevant dominant wavelengths vary from 554 to 607 nm. The related CCTs decrease from 5507 to 1798 T at first and then increase to 2556 T (Table S6), which indicates that the relatively low CCTs can be acquired by tuning the Eu^{3+}/Tb^{3+} proportion. What's more, under the blue UV light photo-

DOI: 10.1021/acs.inorgchem.9b02903
Inorg. Chem. 2020, 59, 648–660

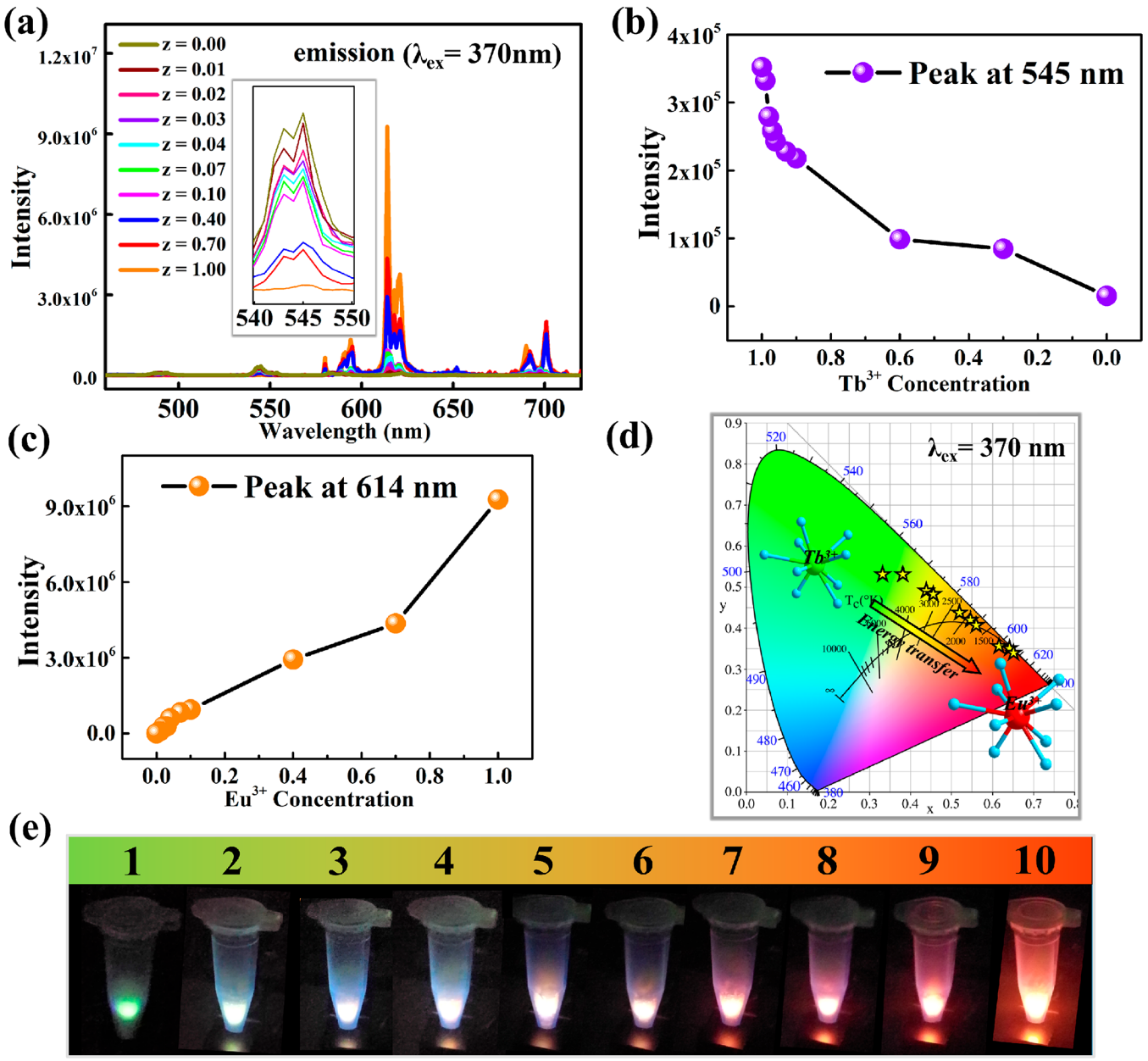

Figure 11. (a) Emission spectra of $Tb_{4-4z}Eu_{4z}W_8$ (z = 0.00, 0.01, 0.02, 0.03, 0.04, 0.07, 0.10, 0.40, 0.70, 1.00) upon λ_{ex} = 370 nm. (b) The relation between the concentration of Tb^{3+} ions and the emission intensity of the peak at 545 nm upon λ_{ex} = 370 nm in $Tb_{4-4z}Eu_{4z}W_8$. (c) The relation between the concentration of Eu^{3+} ions and the emission intensity of the peak at 614 nm upon λ_{ex} = 370 nm in $Tb_{4-4z}Eu_{4z}W_8$. (d) CIE 1937 coordinates of $Tb_{4-4z}Eu_{4z}W_8$ upon λ_{ex} = 370 nm. (e) Experimental pictures of emitting color upon λ_{ex} = 370 nm for $Tb_{4-4z}Eu_{4z}W_8$.

excitation, the tunable and visible emission property with the variation from green to red of $Tb_{4-4z}Eu_{4z}W_8$ (z = 0.00, 0.01, 0.02, 0.03, 0.04, 0.07, 0.10, 0.40, 0.70, 1.00) have been realized (Figure 11e). $Tb_{3.92}Eu_{0.08}W_8$ generates a near-white-light emission through combining upon excitation at 370 nm (Figure 11e) with an excellent CCT of 3518 K, which shows a great potential to act as phosphor for W-LEDs.[56]

Under irradiation of the UV lamp at 396 nm, the emission spectra, the CIE color coordinates, and experimental luminous pictures of $Tb_{4-4z}Eu_{4z}W_8$ (z = 0.00, 0.01, 0.02, 0.03, 0.04, 0.07, 0.10, 0.40, 0.70, 1.00) are also recorded and generated only languishing red emissions (Figure S10, Table S7).

CONCLUSIONS

To sum up, a double-oxalate-bridging tetra-Gd substituted dimeric isopolytungtate Gd_4W_8 was isolated and is composed of two divacant Lindqvist [W_4] segments, four Gd^{3+} ions, and two oxalate ligands. When Na^+ cations perform as metal linkers, picturesque 1-D sinusoidal Na−O cluster chains are formed by self-aggregation of Na^+ ions. In the help of the bridging role of 1-D sinusoidal Na−O cluster chains, Gd_4W_8-**1** POAs are linked together to produce a 3-D multichannel framework. When codoping Eu^{3+} ions and Tb^{3+} ions in Gd_4W_8, the Tb^{3+} to Eu^{3+} ET phenomenon has been investigated under excitation at 370 nm. The ET mechanism has been confirmed as a nonradiative dipole−dipole interaction. The tunable emission property is successfully realized by exciting $Tb_{4-4z}Eu_{4z}W_8$ (z = 0.00, 0.01, 0.02, 0.03, 0.04,

DOI: 10.1021/acs.inorgchem.9b02903
Inorg. Chem. 2020, 59, 648−660

0.07, 0.10, 0.40, 0.70, 1.00), where $Tb_{3.92}Eu_{0.08}W_8$ gives out a near-white-light emission under excitation at 370 nm with an excellent CCT of 3518 K. From the above-mentioned luminous performance analysis, it can be thought that hetero-Ln codoped POM materials may be of great significance for the design and application of color-tunable POM-based materials. In the future, we will concentrate on the search and exploitation of hetero-Ln codoped POM-based luminescent materials with the aim at discovering novel POMIOHMs bearing special structures and eminent performances.

■ ASSOCIATED CONTENT

Supporting Information

The Supporting Information is available free of charge at https://pubs.acs.org/doi/10.1021/acs.inorgchem.9b02903.

Physical measurements; preparations and characterization of Eu^{3+} and/or Tb^{3+} codoped Gd_4W_8 systems; some crystal data of Gd_4W_8; some figures involving structure, IR, and TG curves; and related and luminescence properties (PDF)

Accession Codes

CCDC 1949624 contains the supplementary crystallographic data for this paper. These data can be obtained free of charge via www.ccdc.cam.ac.uk/data_request/cif, or by emailing data_request@ccdc.cam.ac.uk, or by contacting The Cambridge Crystallographic Data Centre, 12 Union Road, Cambridge CB2 1EZ, UK; fax: +44 1223 336033.

■ AUTHOR INFORMATION

Corresponding Authors

*E-mail: ljchen@henu.edu.cn.

*E-mail: zhaojunwei@henu.edu.cn.

ORCID

Junwei Zhao: 0000-0002-7685-1309

Notes

The authors declare no competing financial interest.

■ ACKNOWLEDGMENTS

This work was supported by the National Natural Science Foundation of China (21671054, 21871077, 21571048, 21771052), the Program for Innovation Teams in Science and Technology in Universities of Henan Province (20IRTSTHN004), the Program of First-Class Discipline Cultivation Project of Henan University (2019YLZDYJ02), and the Program for National Innovative Experimental Training for College Students (201910475034).

■ REFERENCES

(1) Dolbecq, A.; Dumas, E.; Mayer, C. R.; Mialane, P. Hybrid organic-inorganic polyoxometalate compounds: from structural diversity to applications. *Chem. Rev.* **2010**, *110*, 6009−6048.

(2) Chen, Y. H.; Sun, L. H.; Chang, S. Z.; Chen, L. J.; Zhao, J. W. Synergistic effect between different coordination geometries of lanthanides and various coordination modes of 2-picolinic acid ligands tuning three types of rare 3d−4f heterometallic tungstoantimonates. *Inorg. Chem.* **2018**, *57*, 15079−15092.

(3) Hu, T.-P.; Zhao, Y.-Q.; Jaglicic, Z.; Yu, K.; Wang, X.-P.; Sun, D. Four hybrid materials based on Preyssler P_5W_{30} polyoxometalate and first-row transition-metal complex. *Inorg. Chem.* **2015**, *54*, 7415−7423.

(4) Ma, F. J.; Liu, S. X.; Sun, C. Y.; Liang, D. D.; Ren, G. J.; Wei, F.; Chen, Y. G.; Su, Z. M. A sodalite-type porous metal-organic framework with polyoxometalate templates: adsorption and decomposition of dimethyl methylphosphonate. *J. Am. Chem. Soc.* **2011**, *133*, 4178−4181.

(5) Blazevic, A.; Rompel, A. The Anderson−Evans polyoxometalate: from inorganic building blocks via hybrid organic−inorganic structures to tomorrows "bio-POM. *Coord. Chem. Rev.* **2016**, *307*, 42−64.

(6) Li, Y.-W.; Guo, L.-Y.; Su, H.-F.; Jagodič, M.; Luo, M.; Zhou, X.-Q.; Zeng, S.-Y.; Tung, C.-H.; Sun, D.; Zheng, L.-S. Two unprecedented POM-based inorganic−organic hybrids with concomitant heteropolytungstate and molybdate. *Inorg. Chem.* **2017**, *56*, 2481−2489.

(7) Long, D.-L.; Abbas, H.; Kögerler, P.; Cronin, L. A high-nuclearity "celtic-ring" isopolyoxotungstate, $[H_{12}W_{36}O_{120}]^{12-}$, that captures trace potassium ions. *J. Am. Chem. Soc.* **2004**, *126*, 13880−13881.

(8) Liu, J. C.; Luo, J.; Han, Q.; Cao, J.; Chen, L. J.; Song, Y.; Zhao, J. W. Coexistence of long-range ferromagnetic ordering and spin-glass behavior observed in the first inorganic−organic hybrid 1-D oxalate-bridging nona-Mn^{II} sandwiched tungstoantimonate chain. *J. Mater. Chem. C* **2017**, *5*, 2043−2055.

(9) Wang, S. S.; Yang, G. Y. Recent advances in polyoxometalate-catalyzed reactions. *Chem. Rev.* **2015**, *115*, 4893−4962.

(10) Shang, S. X.; Lin, Z. G.; Yin, A. X.; Yang, S.; Chi, Y. N.; Wang, Y.; Dong, J.; Liu, B.; Zhen, N.; Hill, C. L.; Hu, C. W. Self-assembly of Ln(III)-containing tungstotellurates(VI): correlation of structure and photoluminescence. *Inorg. Chem.* **2018**, *57*, 8831−8840.

(11) Raula, M.; Gan Or, G.; Saganovich, M.; Zeiri, O.; Wang, Y.; Chierotti, M. R.; Gobetto, R.; Weinstock, I. A. Polyoxometalate complexes of anatase-titanium dioxide cores in water. *Angew. Chem., Int. Ed.* **2015**, *54*, 12416−12421.

(12) Gupta, R.; Khan, I.; Hussain, F.; Bossoh, A. M.; Mbomekalle, I. M.; de Oliveira, P.; Sadakane, M.; Kato, C.; Ichihashi, K.; Inoue, K.; Nishihara, S. Two new sandwich-type manganese $\{Mn_5\}$-substituted polyoxotungstates: syntheses, crystal structures, electrochemistry, and magnetic properties. *Inorg. Chem.* **2017**, *56*, 8759−8767.

(13) Li, H. L.; Liu, Y. J.; Liu, J. L.; Chen, L. J.; Zhao, J. W.; Yang, G. Y. Structural transformation from dimerization to tetramerization of serine-decorated rare-earth-incorporated arsenotungstates induced by the usage of rare-earth salts. *Chem. - Eur. J.* **2017**, *23*, 2673−2689.

(14) Luo, X.-M.; Li, N.-F.; Hu, Z.-B.; Cao, J.-P.; Cui, C.-H.; Lin, Q.-F.; Xu, Y. Polyoxometalate-based well-defined rodlike structural multifunctional materials: synthesis, structure, and properties. *Inorg. Chem.* **2019**, *58*, 2463−2470.

(15) Wang, J.; Liang, Y. F.; Ma, P. T.; Zhang, D. D.; Niu, J. Y.; Wang, J. P. Ligand-controlled formation of covalently modified antimonio-molybdates and their photochromic properties. *CrystEngComm* **2017**, *19*, 207−213.

(16) Song, Y.-F.; Cronin, L. Postsynthetic covalent modification of metal−organic framework (MOF) materials. *Angew. Chem., Int. Ed.* **2008**, *47*, 4635−4637.

(17) Wee, L. H.; Wiktor, C.; Turner, S.; Vanderlinden, W.; Janssens, N.; Bajpe, S. R.; Houthoofd, K.; Van Tendeloo, G.; De Feyter, S.; Kirschhock, C. E. A.; Martens, J. A. Copper benzene tricarboxylate metal−organic framework with wide permanent mesopores stabilized by Keggin polyoxometalate ions. *J. Am. Chem. Soc.* **2012**, *134*, 10911−10919.

(18) Cai, J.; Zheng, X. Y.; Xie, J.; Yan, Z. H.; Kong, X. J.; Ren, Y. P.; Long, L. S.; Zheng, L. S. Anion-dependent assembly of heterometallic 3d−4f clusters based on a lacunary polyoxometalate. *Inorg. Chem.* **2017**, *56*, 8439−8445.

(19) Han, Q.; Liu, J.-C.; Wen, Y.; Chen, L.-J.; Zhao, J.-W.; Yang, G.-Y. Tellurotungstate-based organotin−rare-earth heterometallic hybrids with four organic components. *Inorg. Chem.* **2017**, *56*, 7257−7269.

(20) Li, D. D.; Xu, Q. F.; Li, Y. G.; Qiu, Y. T.; Ma, P. T.; Niu, J. Y.; Wang, J. P. A stable polyoxometalate-based metal−organic framework

DOI: 10.1021/acs.inorgchem.9b02903
Inorg. Chem. 2020, 59, 648−660

as highly efficient heterogeneous catalyst for oxidation of alcohols. *Inorg. Chem.* **2019**, *58*, 4945−4953.
(21) Zhang, Z.-M.; Duan, X. P.; Yao, S.; Wang, Z. S.; Lin, Z. K.; Li, Y.-G.; Long, L.-S.; Wang, E.-B.; Lin, W. B. Cation-mediated optical resolution and anticancer activity of chiral polyoxometalates built from entirely achiral building blocks. *Chem. Sci.* **2016**, *7*, 4220−4229.
(22) Wang, Y.-J.; Wu, S.-Y.; Sun, Y.-Q.; Li, X.-X.; Zheng, S.-T. Octahedron-shaped three-shell Ln_{14}-substituted polyoxotungsto-germanates encapsulating a W_4O_{15} cluster: luminescence and frequency dependent magnetic properties. *Chem. Commun.* **2019**, *55*, 2857−2860.
(23) Mialane, P.; Dolbecq, A.; Rivière, E.; Marrot, J.; Sécheresse, F. Functionalization of polyoxometalates by a negatively charged bridging ligand: the dimeric $[(SiW_{11}O_{39}Ln)_2(\mu\text{-}CH_3COO)_2]^{12-}$ (Ln = Gd^{III}, Yb^{III}) complexes. *Eur. J. Inorg. Chem.* **2004**, *2004*, 33−36.
(24) Ritchie, C.; Boskovic, C. Disassembly and reassembly of polyoxometalates: the formation of chains from an adaptable precursor. *Cryst. Growth Des.* **2010**, *10*, 488−491.
(25) Niu, J. Y.; Wang, K. H.; Chen, H. N.; Zhao, J. W.; Ma, P. T.; Wang, J. P.; Li, M. X.; Bai, Y.; Dang, D. B. Assembly chemistry between lanthanide cations and monovacant Keggin polyoxotungstates: two types of lanthanide substituted phosphotungstates $[\{(\alpha\text{-}PW_{11}O_{39}H)Ln(H_2O)_3\}_2]^{6-}$ and $[\{(\alpha\text{-}PW_{11}O_{39})\ Ln(H_2O)(\eta^2,\mu\text{-}1,1)\text{-}CH_3COO\}_2]^{10-}$. *Cryst. Growth Des.* **2009**, *9*, 4362−4372.
(26) An, H. Y.; Han, Z. B.; Xu, T. Q. Three-dimensional architectures based on lanthanide-substituted double Keggin-type polyoxometalates and lanthanide cations or lanthanide-organic complexes. *Inorg. Chem.* **2010**, *49*, 11403−11414.
(27) Ritchie, C.; Speldrich, M.; Gable, R. W.; Sorace, L.; Kögerler, P.; Boskovic, C. Utilizing the adaptive polyoxometalate $[As_2W_{19}O_{67}(H_2O)]^{14-}$ to support a polynuclear lanthanoid-based single-molecule magnet. *Inorg. Chem.* **2011**, *50*, 7004−7014.
(28) Ritchie, C.; Baslon, V.; Moore, E. G.; Reber, C.; Boskovic, C. Sensitization of lanthanoid luminescence by organic and inorganic ligands in lanthanoid-organic-polyoxometalates. *Inorg. Chem.* **2012**, *51*, 1142−1151.
(29) Ibrahim, M.; Mal, S. S.; Bassil, B. S.; Banerjee, A.; Kortz, U. Yttrium(III)-containing tungstoantimonate(III) stabilized by tetrahedral WO_4^{2-} capping unit, $[\{Y(\alpha\text{-}SbW_9O_{31}(OH)_2)(CH_3COO)(H_2O)\}_3(WO_4)]^{17-}$. *Inorg. Chem.* **2011**, *50*, 956−960.
(30) An, H. Y.; Zhang, Y. M.; Hou, Y. J.; Hu, T.; Yang, W.; Chang, S. Z.; Zhang, J. J. Hybrid dimers based on metal-substituted Keggin polyoxometalates (metal = Ti, Ln) for cyanosilylation catalysis. *Dalton Trans.* **2018**, *47*, 9079−9089.
(31) Wu, H. C.; Zhi, M. N.; Singh, V.; Li, H. F.; Ma, P. T.; Niu, J. Y.; Wang, J. P. Elucidating white light-emitting emissions in Tm^{3+}/Dy^{3+} codoped polyoxometalates: a color-tunable and energy transfer mechanism study. *Dalton Trans.* **2018**, *47*, 13949−13956.
(32) Luo, X.-M.; Li, N.-F.; Hu, Z.-B.; Cao, J.-P.; Cui, C.-H.; Lin, Q.-F.; Xu, Y. Polyoxometalate-based well-defined rodlike structural multifunctional materials: synthesis, structure, and properties. *Inorg. Chem.* **2019**, *58*, 2463−2470.
(33) Li, Y. M.; Li, H. L.; Jiang, J.; Chen, L. J.; Zhao, J. W. Three types of distinguishing L-alanine-decorated and rare-earth-incorporated arsenotungstate hybrids prepared in a facile one step assembly strategy. *Inorg. Chem.* **2019**, *58*, 3479−3491.
(34) Liu, C.; Luo, F.; Liu, N.; Cui, Y.; Wang, Xi.; Wang, E. B.; Chen, J. One-dimensional helical chain based on decatungstate and cerium organic-inorganic hybrid material. *Cryst. Growth Des.* **2006**, *6*, 2658−2660.
(35) Zhao, J.-W.; Li, Y.-Z.; Chen, L.-J.; Yang, G.-Y. Research progress on polyoxometalate-based transition-metal-rare-earth heterometallic derived materials: synthetic strategies, structural overview and functional applications. *Chem. Commun.* **2016**, *52*, 4418−4445.
(36) Armelao, L.; Quici, S.; Barigelletti, F.; Accorsi, G.; Bottaro, G.; Cavazzini, M.; Tondelloe, E. Design of luminescent lanthanide complexes: from molecules to highly efficient photo-emitting materials. *Coord. Chem. Rev.* **2010**, *254*, 487−505.
(37) Artetxe, B. Systematic studies on 3d- and 4f-metal containing polyoxometalates suitable for organic derivatization. *ChemistryOpen* **2016**, *5*, 261−266.
(38) Yamase, T. Photo- and electrochromism of polyoxometalates and related materials. *Chem. Rev.* **1998**, *98*, 307.
(39) Zhang, J.; Cai, G. M.; Yang, L. W.; Ma, Z. Y.; Jin, Z. P. Layered crystal structure, color-tunable photoluminescence, and excellent thermal stability of $MgIn_2P_4O_{14}$ phosphate-based phosphors. *Inorg. Chem.* **2017**, *56*, 12902−12913.
(40) Wei, T.; Tian, Y.; Tian, C.; Cai, M. Z.; Jing, X. F.; Li, B. P.; Chen, R.; Zhang, J. J.; Xu, S. Q. Quantitative analysis of energy transfer and origin of quenching in Er^{3+}/Ho^{3+} codoped germanosilicate glasses. *J. Phys. Chem. A* **2015**, *119*, 6823−6830.
(41) Oh, J. H.; Oh, J. R.; Park, H. K.; Sung, Y.-G.; Do, Y. R. New paradigm of multi-chip white LEDs: combination of an InGaN blue LED and full down-converted phosphor-converted LEDs. *Opt. Express* **2011**, *19*, A270−A279.
(42) Min, X.; Huang, Z.; Fang, M.; Liu, Y.; Tang, C.; Wu, X. Energy transfer from Sm^{3+} to Eu^{3+} in red-emitting phosphor $LaMgAl_{11}O_{19}:Sm^{3+}$, Eu^{3+} for solar cells and near-ultraviolet white light-emitting diodes. *Inorg. Chem.* **2014**, *53*, 6060−6065.
(43) Wu, H.; Yan, B.; Li, H.; Singh, V.; Ma, P.; Niu, J.; Wang, J. Enhanced photostability luminescent properties of Er^{3+}-doped near-white-emitting $Dy_xEr_{(1-x)}$-POM derivatives. *Inorg. Chem.* **2018**, *57*, 7665−7675.
(44) Liu, J.-L.; Jin, M.-T.; Chen, L.-J.; Zhao, J.-W. First dimethyltin-functionalized rare-earth incorporated tellurotungstates consisting of $\{B\text{-}\alpha\text{-}TeW_7O_{28}\}$ and $\{W_5O_{18}\}$ mixed building units. *Inorg. Chem.* **2018**, *57*, 12509−12520.
(45) Zhang, Y.; Gong, W. T.; Yu, J. J.; Lin, Y.; Ning, G. L. Tunable white-light emission via energy transfer in single-phase $LiGd(WO_4)_2:Re^{3+}$ (Re = Tm, Tb, Dy, Eu) phosphors for UV-excited WLEDs. *RSC Adv.* **2015**, *5*, 96272−96280.
(46) Shi, R.; Liu, G. K.; Liang, H. B.; Huang, Y.; Tao, Y.; Zhang, J. Consequences of ET and MMCT on Luminescence of Ce^{3+}-, Eu^{3+}-, and Tb^{3+}-doped $LiYSiO_4$. *Inorg. Chem.* **2016**, *55*, 7777−7786.
(47) Tian, B.; Chen, B.; Tian, Y.; Li, X.; Zhang, J.; Sun, J.; Zhong, H.; Cheng, L.; Fu, S.; Zhong, H.; Wang, Y.; Zhang, X.; Xia, H.; Hua, R. Excitation pathway and temperature dependent luminescence in color tunable $Ba_5Gd_8Zn_4O_{21}:Eu^{3+}$ phosphors. *J. Mater. Chem. C* **2013**, *1*, 2338−2344.
(48) Vijayakumar, R.; Guo, H.; Huang, X. Y. Energy transfer and color-tunable luminescence properties of Dy^{3+} and Eu^{3+} co-doped $Na_3Sc_2(PO_4)_3$ phosphors for near-UV LED-based warm white LEDs. *Dyes Pigm.* **2018**, *156*, 8−16.
(49) Geng, D. L.; Li, G. G.; Shang, M. M.; Peng, C.; Zhang, Y.; Cheng, Z. Y.; Lin, J. Nanocrystalline $CaYAlO_4:Tb^{3+}/Eu^{3+}$ as promising phosphors for full-color field emission displays. *Dalton Trans.* **2012**, *41*, 3078−3086.
(50) Guan, H.; Sheng, Y.; Song, Y.; Xu, C.; Zhou, X.; Zheng, K.; Shi, Z.; Zou, H. $YF_3:RE^{3+}$ (RE = Dy, Tb, Eu) Sub-microstructures: controllable morphology, tunable multicolor, and thermal properties. *J. Phys. Chem. C* **2017**, *121*, 23080−23095.
(51) Yamase, T. Chapter 243, luminescence of polyoxometallolanthanoates and photochemical nano-ring formation. *Handbook of the Physics and Chemistry of Rare Earths*; Gschneider, K. A., Bünzli, Jr., J. C. G., Pecharsky, V. K., Eds.; Elsevier: 2009; Vol. *39*, pp 297−356.
(52) Yamase, T.; Naruke, H. Luminescence and energy transfer phenomena in Tb^{3+}/Eu^{3+}-mixed polyoxometallolanthanoates $K_{15}H_3[Tb_{1.4}Eu_{1.6}(H_2O)_3(SbW_9O_{33})(W_5O_{18})_3]\cdot 25.5H_2O$ and $Na_7H_{19}[Tb_{4.3}\text{-}Eu_{1.7}\ O_2(OH)_6(H2O)_6Al_2(Nb_6O_{19})_5]\cdot 47H_2O$. *J. Phys. Chem. B* **1999**, *103*, 8850−8857.
(53) Xia, M.; Wu, X. B.; Zhong, Y.; Hintzen, H. T.; Zhou, Z.; Wang, J. Photoluminescence properties and energy transfer in a novel $Sr_8ZnY(PO_4)_7:Tb^{3+},Eu^{3+}$ phosphor with high thermal stability and its great potential for application in warm white light emitting diodes. *J. Mater. Chem. C* **2019**, *7*, 2927−2935.
(54) Xin, M.; Tu, D.; Zhu, H.; Luo, W.; Liu, Z.; Huang, P.; Li, R.; Cao, Y.; Chen, X. Single-composition white-emitting $NaSrBO_3:Ce^{3+}$,

DOI: 10.1021/acs.inorgchem.9b02903
Inorg. Chem. 2020, 59, 648−660

Sm^{3+},Tb^{3+} phosphors for NUV light-emitting diodes. *J. Mater. Chem. C* **2015**, *3*, 7286−7293.
(55) Zhao, J. W.; Li, H. L.; Li, Y. Z.; Li, C. Y.; Wang, Z. L.; Chen, L. J. Rectangle versus square oxalate-connective tetralanthanide cluster anchored in lacunary Lindqvist isopolytungstates: syntheses, structures, and properties. *Cryst. Growth Des.* **2014**, *14*, 5495−5505.
(56) Ying, J.; Chen, Y.-G.; Wang, X.-Y. Two isopolytungstate compounds based on rare $[W_6O_{22}]^{8-}$ and $[H_2W_{12}O_{42}]^{10-}$ fragments captured by premade copper(ii) complexes. *New J. Chem.* **2019**, *43*, 6765−6771.
(57) Cai, J.; Zheng, X.-Y.; Xie, J.; Yan, Z.-H.; Kong, X.-J.; Ren, Y. −P.; Long, L.-S.; Zheng, L.-S. Anion-dependent assembly of heterometallic 3d−4f clusters based on a lacunary polyoxometalate. *Inorg. Inorg. Chem.* **2017**, *56*, 8439−−8445.
(58) Zhao, J.-W.; Cao, J.; Li, Y.-Z.; Zhang, J.; Chen, L.-J. First tungstoantimonate-based transition-metal−lanthanide heterometallic hybrids functionalized by amino acid ligands. *Cryst. Growth Des.* **2014**, *14*, 6217−6229.
(59) Bordiga, S.; Damin, A.; Bonino, F.; Zecchina, A.; Spanò, G.; Rivetti, F.; Bolis, V.; Prestipino, C.; Lamberti, C. Effect of interaction with H_2O and NH_3 on the vibrational, electronic, and energetic peculiarities of Ti(IV) centers TS-1 catalysts: a spectroscopic and computational study. *J. Phys. Chem. B* **2002**, *106*, 9892−9905.
(60) Szeto, K. C.; Lillerud, K. P.; Tilset, M.; Bjørgen, M.; Prestipino, C.; Zecchina, A.; Lamberti, C.; Bordiga, S. A thermally stable Pt/Y-based metal−organic framework: exploring the accessibility of the metal centers with spectroscopic methods using H_2O, CH_3OH, and CH_3CN as probes. *J. Phys. Chem. B* **2006**, *110*, 21509−21520.
(61) Zhao, J. W.; Wang, C. M.; Zhang, J.; Zheng, S. T.; Yang, G. Y. Combination of lacunary polyoxometalates and high-nuclear transition metal clusters under hydrothermal conditions: IX. a series of novel polyoxotungstates sandwiched by octa-copper clusters. *Chem. - Eur. J.* **2008**, *14*, 9223−9239.
(62) Zhao, J. W.; Li, H. L.; Li, Y. Z.; Li, C. Y.; Wang, Z. L.; Chen, L. J. Rectangle versus square oxalate-connective tetralanthanide cluster anchored in lacunary lindqvist isopolytungstates: syntheses, structures, and properties. *Cryst. Growth Des.* **2014**, *14*, 5495−5505.
(63) Zhou, J.-M.; Li, H.-H.; Zhang, H.; Li, H.-M.; Shi, W.; Cheng, P. A bimetallic lanthanide metal-organic material as a self-calibrating color-gradient luminescent sensor. *Adv. Mater.* **2015**, *27*, 7072−7077.
(64) Zhao, D.; Rao, X.-T.; Yu, J.-C.; Cui, Y.-J.; Yang, Y.; Qian, G.-D. Design and synthesis of an MOF thermometer with high sensitivity in the physiological temperature range. *Inorg. Chem.* **2015**, *54*, 11193−11199.
(65) Zhou, W. J.; Gu, M.; Ou, Y. Y.; Zhang, C. H.; Zhang, X. J.; Zhou, L.; Liang, H. B. Concentration-driven selectivity of energy transfer channels and color tunability in $Ba_3La(PO_4)_3$:Tb^{3+}, Sm^{3+} for warm white LEDs. *Inorg. Chem.* **2017**, *56*, 7433−7442.
(66) Liu, Y.; Liu, G. X.; Wang, J. X.; Dong, X. T.; Yu, W. S. Single-component and warm-white-emitting phosphor $NaGd(WO_4)_2$:Tm^{3+}, Dy^{3+}, Eu^{3+}: synthesis, luminescence, energy transfer, and tunable color. *Inorg. Chem.* **2014**, *53*, 11457−11466.
(67) Praveena, R.; Sameera, V. S.; Babu, P.; Basavapoornima, C.; Jayasankar, C. K. Photoluminescence properties of Ho^{3+}/Tm^{3+}-doped YAGG nanocrystalline powders. *Opt. Mater.* **2017**, *72*, 666−672.
(68) Wu, Y. M.; Cen, Y.; Huang, L. J.; Yu, R. Q.; Chu, X. Upconversion fluorescence resonance energy transfer biosensor for sensitive detection of human immunodeficiency virus antibodies in human serum. *Chem. Commun.* **2014**, *50*, 4759−4762.
(69) Guan, H.; Sheng, Y.; Song, Y.; Xu, C.; Zhou, X.; Zheng, K.; Shi, Z.; Zou, H. YF_3:RE^{3+} (RE = Dy, Tb, Eu) Sub-microstructures: controllable morphology, tunable multicolor, and thermal properties. *J. Phys. Chem. C* **2017**, *121*, 23080−23095.
(70) Carrasco, I.; Piccinelli, F.; Romet, I.; Nagirnyi, V.; Bettinelli, M. Competition between energy transfer and energy migration processes in neat and Eu^{3+}-Doped $TbPO_4$. *J. Phys. Chem. C* **2018**, *122*, 6858−6864.
(71) Gupta, S. K.; Ghosh, P. S.; Yadav, A. K.; Pathak, N.; Arya, A.; Jha, S. N.; Bhattacharyya, D.; Kadam, R. M. Luminescence properties of $SrZrO_3$/Tb^{3+} perovskite: host-dopant energy-transfer dynamics and local structure of Tb^{3+}. *Inorg. Chem.* **2016**, *55*, 1728−1740.
(72) Peng, C.; Li, C.; Li, G.; Li, S.; Lin, J. YF_3:Ln^{3+} (Ln = Ce, Tb, Pr) submicrospindles: hydrothermal synthesis and luminescence properties. *Dalton Trans.* **2012**, *41*, 8660−8668.
(73) Zhou, X.; Wang, H.; Jiang, S.; Xiang, G.; Tang, X.; Luo, X.; Li, L.; Zhou, X. Multifunctional Luminescent material Eu(III) and Tb(III) complexes with pyridine-3,5-dicarboxylic acid linker: crystal structures, tunable emission, energy transfer, and temperature sensing. *Inorg. Chem.* **2019**, *58*, 3780−3788.
(74) Kang, F. W.; Sun, G. H.; Wang, A. W.; Xiao, X. F.; Li, Y. Y.; Lu, J.; Huang, B. L. Multicolor tuning and temperature-triggered anomalous Eu^{3+}-related photoemission enhancement via interplay of accelerated energy transfer and release of defect-trapped electrons in the Tb^{3+}, Eu^{3+}-doped strontium−aluminum chlorites. *ACS Appl. Mater. Interfaces* **2018**, *10*, 36157−36170.
(75) Wu, L.; Zhang, Y.; Gui, M. Y.; Lu, P. Z.; Zhao, L. X.; Tian, S.; Kong, Y. F.; Xu, J. J. Luminescence and energy transfer of a color tunable phosphor: Dy^{3+}-, Tm^{3+}-, and Eu^{3+}-coactivated $KSr_4(BO_3)_3$ for warm white UV LEDs. *J. Mater. Chem.* **2012**, *22*, 6463−6470.
(76) Huang, C.-H; Chen, T.-M. Novel yellow-emitting $Sr_8MgLn(PO_4)_7$:Eu^{2+} (Ln = Y, La) phosphors for applications in white LEDs with excellent color rendering index. *Inorg. Chem.* **2011**, *50*, 5725−5730.
(77) Li, H.; Zhao, R.; Jia, Y.; Sun, W.; Fu, J.; Jiang, L.; Zhang, S.; Pang, R.; Li, C. $Sr_{1.7}Zn_{0.3}CeO_4$: Eu^{3+} novel red-emitting phosphors: synthesis and photoluminescence properties. *ACS Appl. Mater. Interfaces* **2014**, *6*, 3163−3169.
(78) Pang, M. L.; Lin, J.; Fu, J.; Xing, R. B.; Luo, C. X.; Han, Y. C. Preparation, patterning and luminescent properties of nanocrystalline Gd_2O_3:A (A = Eu^{3+}, Dy^{3+}, Sm^{3+}, Er^{3+}) phosphor films via pechini sol−gel soft lithography. *Opt. Mater.* **2003**, *23*, 547−558.
(79) Yu, C. C.; Liu, X. M.; Yu, M.; Lin, C. K.; Li, C. X.; Wang, H.; Lin, J. Enhanced photoluminescence of Ba_2GdNbO_6:Eu^{3+}/Dy^{3+} phosphors by Li^+ doping. *J. Solid State Chem.* **2007**, *180*, 3058−3065.
(80) Zhang, X.; Zhou, L.; Pang, Q.; Shi, J.; Gong, M. Tunable luminescence and Ce^{3+}→Tb^{3+}→Eu^{3+} energy transfer of broadband-excited and narrow line red emitting Y_2SiO_5:Ce^{3+}, Tb^{3+}, Eu^{3+} phosphor. *J. Phys. Chem. C* **2014**, *118*, 7591−7598.
(81) Geng, D.; Shang, M.; Zhang, Y.; Cheng, Z.; Lin, J. Tunable and white-light emission from single-phase $Ca_2YF_4PO_4$:Eu^{2+},Mn^{2+} phosphors for application in W-LEDs. *Eur. J. Inorg. Chem.* **2013**, *2013*, 2947−2953.
(82) Huang, C.-H.; Wu, P.-J.; Lee, J.-F.; Chen, T.-M. $(Ca,Mg,Sr)_9Y(PO_4)_7$:Eu^{2+},Mn^{2+}: Phosphors for white-light near-UV LEDs through crystal field tuning and energy transfer. *J. Mater. Chem.* **2011**, *21*, 10489−10495.
(83) Dexter, D. L.; Schulman, J. A. Theory of concentration quenching in inorganic phosphors. *J. Chem. Phys.* **1954**, *22*, 1063−1070.
(84) Blasse, G. Energy transfer in oxidic phosphors. *Phys. Lett. A* **1968**, *28*, 444−445.
(85) Blasse, G. Energy transfer between inequivalent Eu^{2+} ions. *J. Solid State Chem.* **1986**, *62*, 207−211.
(86) Kang, F.; Li, L.; Han, J.; Lei, D. Y.; Peng, M. Emission color tuning through manipulating the energy transfer from VO_4^{3-} to Eu^{3+} in single-phased LuVO4:Eu^{3+} phosphors. *J. Mater. Chem. C* **2017**, *5*, 390−398.
(87) Decadt, R.; Van Hecke, K.; Depla, D.; Leus, K.; Weinberger, D.; Van Driessche, I.; Van Der Voort, P.; Van Deun, R. Synthesis, crystal structures, and luminescence properties of carboxylate based rare-earth coordination polymers. *Inorg. Chem.* **2012**, *51*, 11623−11634.
(88) Li, K.; Liang, S. S.; Shang, M. M.; Lian, H. Z.; Lin, J. Photoluminescence and energy transfer properties with Y+SiO_4 Substituting Ba+PO_4 in $Ba_3Y(PO_4)_3$:Ce^{3+}/Tb^{3+}, Tb^{3+}/Eu^{3+} Phosphors for w-LEDs. *Inorg. Chem.* **2016**, *55*, 7593−7604.

DOI: 10.1021/acs.inorgchem.9b02903
Inorg. Chem. 2020, 59, 648−660

(89) Jiao, H.; Liao, F.; Tian, S.; Jing, X. Luminescent properties of Eu^{3+} and Tb^{3+} activated $Zn_3Ta_2O_8$. *J. Electrochem. Soc.* **2003**, *150*, H220−H224.
(90) Wang, Q.; Xu, H. S.; Zhang, F. Z.; Wang, Z. H. Influence of color temperature on comfort and preference for LED indoor lighting. *Optik* **2017**, *129*, 21−29.
(91) Kapogiannatou, A.; Paronis, E.; Paschidis, K.; Polissidis, A.; Kostomitsopoulos, N. G. Effect of light colour temperature and intensity on *τhε* behaviour of male C57CL/6J mice. *Appl. Anim. Behav. Sci.* **2016**, *184*, 135−140.
(92) Zhang, Y.; Gong, W.; Yu, J.; Pang, H.; Song, Q.; Ning, G. A new single -phase white-light-emitting $CaWO_4:Dy^{3+}$ phosphor: synthesis, luminescence and energy transfer. *RSC Adv.* **2015**, *5*, 62527−62533.
(93) Suresh Kumar, J.; Pavani, K.; Mohan Babu, A.; Kumar Giri, N.; Rai, S.B.; Moorthy, L. R. Fluorescence characteristics of Dy^{3+} ions in calcium fluoroborate glasses. *J. Lumin.* **2010**, *130*, 1916−1923.
(94) McCamy, C. S. Correlated color temperature as an explicit function of chromaticity coordinates. *Color Res. Appl.* **1992**, *17*, 142−144.
(95) Xu, X.; Chen, Y. H.; Zhang, Y.; Liu, Y. F.; Chen, L. J.; Zhao, J. W. Rare-earth and antimony-oxo clusters simultaneously connecting antimonotungstates comprising divacant and tetravacant Keggin fragments. *Inorg. Chem.* **2019**, *58*, 11636−11648.

DOI: 10.1021/acs.inorgchem.9b02903
Inorg. Chem. 2020, 59, 648−660